

## THE EVOLUTION OF EARLY- AND LATE-TYPE GALAXIES IN THE COSMIC EVOLUTION SURVEY UP TO $z \approx 1.2^*$

MAURILIO PANNELLA<sup>1,2</sup>, ARMIN GABASCH<sup>1,3</sup>, YULIANA GORANOVA<sup>4,5,6,7</sup>, NIV DRORY<sup>1</sup>, ULRICH HOPP<sup>1,4</sup>, STEFAN NOLL<sup>1,8</sup>,  
ROBERTO P. SAGLIA<sup>1</sup>, VERONICA STRAZZULLO<sup>2</sup>, AND RALF BENDER<sup>1,4</sup>

<sup>1</sup> Max-Planck-Institut für extraterrestrische Physik, Giessenbachstrasse, Postfach 1312, D-85741 Garching bei München, Germany

<sup>2</sup> National Radio Astronomy Observatory, P.O. Box 0, Socorro, NM 87801-0387, USA; [mpannell@nrao.edu](mailto:mpannell@nrao.edu)

<sup>3</sup> European Southern Observatory, Karl Schwarzschild Strasse 2, Garching bei München, Germany

<sup>4</sup> Universitätssternwarte München, Scheinerstrasse 1, D-81673 München, Germany

<sup>5</sup> UPMC Univ. Paris 06, UMR7095, Institut d’Astrophysique de Paris, F-75014, Paris, France

<sup>6</sup> CNRS, UMR7095, Institut d’Astrophysique de Paris, F-75014, Paris, France

<sup>7</sup> Institute of Astronomy, Bulgarian Academy of Sciences, 72 Tsarigradsko Chaussee Boulevard, 1784 Sofia, Bulgaria

<sup>8</sup> Observatoire Astronomique de Marseille-Provence (OAMP), 38 rue Frédéric Joliot-Curie, 13388 Marseille cedex 13, France

Received 2009 February 23; accepted 2009 June 17; published 2009 July 27

### ABSTRACT

The Cosmic Evolution Survey (COSMOS) allows for the first time a highly significant census of environments and structures up to redshift 1, as well as a full morphological description of the galaxy population. In this paper we present a study aimed to constrain the evolution, in the redshift range  $0.2 < z < 1.2$ , of the mass content of different morphological types and its dependence on the environmental density. We use a deep multicolor catalog, covering an area of  $\sim 0.7 \text{ deg}^2$  inside the COSMOS field, with accurate photometric redshifts ( $i \lesssim 26.5$  and  $\Delta z / (z_{\text{spec}} + 1) \approx 0.035$ ). We estimate galaxy stellar masses by fitting the multicolor photometry to a grid of composite stellar population models. We quantitatively describe the galaxy morphology by fitting point-spread function convolved Sérsic profiles to the galaxy surface brightness distributions down to  $F814 = 24 \text{ mag}$  for a sample of 41,300 objects. We confirm an evolution of the morphological mix with redshift: the higher the redshift the more disk-dominated galaxies become important. We find that the morphological mix is a function of the local comoving density: the morphology density relation extends up to the highest redshift explored. The stellar mass function of disk-dominated galaxies is consistent with being constant with redshift. Conversely, the stellar mass function of bulge-dominated systems shows a decline in normalization with redshift. Such different behaviors of late-types and early-types stellar mass functions naturally set the redshift evolution of the *transition* mass. We find a population of relatively massive, early-type galaxies, having high specific star formation rate (SSFR) and blue colors which live preferentially in low-density environments. The bulk of massive ( $> 7 \times 10^{10} M_{\odot}$ ) early-type galaxies have similar characteristic ages, colors, and SSFRs independently of the environment they belong to, with those hosting the oldest stars in the universe preferentially belonging to the highest density regions. The whole catalog including morphological information and stellar mass estimates analyzed in this work is made publicly available.

*Key words:* galaxies: evolution – galaxies: fundamental parameters – galaxies: luminosity function, mass function – galaxies: statistics – surveys

*Online-only material:* color figures

### 1. INTRODUCTION

Galaxy formation and evolution have been a very actively debated topic of observational cosmology in the last years. Only recently models and observations are converging toward a unified and coherent picture.

On one side the observations of the universe, with some controversies on the way, have finally agreed that half of the present-day stars was already in place at  $z \approx 1$  and that the same mass deficit affects, within the measured accuracies, the high-mass end: basically, the galaxy stellar mass function evolves from the local determination to redshift 1 only by a normalization factor of about 2. This means that, both at high and at low masses, there is roughly a factor of 2 difference between the comoving number density at redshift 1 and the local value (e.g., Dickinson et al. 2003; Rudnick et al. 2003; Drory et al. 2004b; Bundy et al. 2005; Pannella et al. 2006; Borch et al. 2006; Fontana et al. 2006; Pozzetti et al. 2007; Arnouts et al.

2007; Pérez-González et al. 2008; Cowie & Barger 2008; Drory & Alvarez 2008; Marchesini et al. 2008; Ilbert et al. 2009b). Measurements of the star formation rate (SFR) density over cosmic times (e.g., Giavalisco et al. 2004; Gabasch et al. 2004b; Bouwens et al. 2004; Sawicki & Thompson 2006; Bouwens et al. 2007) are also in good agreement with half of the present-day stars being already born at redshift 1.

On the other side the models, linking the hierarchical growth of dark matter structures to the observed galaxy properties by means of simplified prescriptions for the formation of baryonic systems, predict that galaxies form in a bottom-up fashion by following the cosmological destiny of dark matter halos. Massive galaxies, in these models, assemble most (50%) of their stellar mass via merging at  $z < 1$  (De Lucia et al. 2006), but most of these accretion events are red mergers (i.e., gas-free mergers that imply no induced star formation), which are very difficult to detect from the observational point of view (e.g., Hopkins et al. 2008; Cox et al. 2008). The latest realizations of these models (e.g., Bower et al. 2006; Kitzbichler & White 2007; Cattaneo et al. 2008; Fontanot et al. 2009) have been able to fully reproduce the galaxy stellar mass function up to high

\* Based on observations made with the Advanced Camera for Surveys on board the NASA/ESA *Hubble Space Telescope* (GO Proposal 9822).

redshifts, thus reconciling the theoretical bottom-up assembly of dark matter halos to the claimed top-down assembly of galaxies (e.g., Cimatti et al. 2006).

In *hierarchical* models star formation is supposed to take place only in disk structures and in gas-rich mergers (see also Dekel et al. 2009 for an up to date perspective). This latter event would exhaust the residual gas and create a dynamically hot system: a bulge galaxy. Also dynamical instabilities and minor mergers are able to destroy the disk structures and finally create an elliptical galaxy. Detailed predictions in the literature do not exist but the general expectation is that the fraction of bulge-dominated massive galaxies increases with time.

The study of the evolution of the morphological mix in the galaxy stellar mass function is a decisive tool to put sensitive constraints on the models, because it could give unique insights into both the feedback and the merging processes in galaxy evolution (see for a detailed discussion Cole et al. 2000).

Galaxies have been often classified, both at low and at high redshift, as “red-sequence” and “blue-cloud” objects based on their broadband colors (Baldry et al. 2004; Fontana et al. 2004; Giallongo et al. 2005; Bundy et al. 2006). However, this kind of classification when used as a proxy for the galaxy morphology (see, e.g., Mobasher et al. 2009), suffers from some obvious drawbacks: a disk galaxy populated by an old stellar population would be classified as an early-type object, and vice versa; a starburst galaxy, heavily obscured by dust, would be classified as a red, and *dead*, early-type object.

Thanks to the advent of the Advanced Camera for Surveys (ACS; Ford et al. 2003) on board the *Hubble Space Telescope* (*HST*), it has become possible to investigate the optical rest-frame emission of galaxies up to redshift 1 and slightly beyond with subkiloparsec resolution and on relatively wide fields for hundreds of thousands of galaxies.

Given the exponentially growing number of galaxies available to be morphologically classified it has become urgent for galaxy evolution studies to build up robust and automated tools for morphological and structural classification that could reliably substitute the visual classification (see the discussion in Bamford et al. 2009 on unavoidable drawbacks affecting the automated approach). The efforts on the path to the automated image classification have essentially split in two main branches, parametric and nonparametric methods, each having its own advantages and drawbacks.

Parametric methods are based on the idea that galaxy light profiles may be sufficiently well described by analytic formulae. Indeed parametric profiles have been shown to well describe galaxy structural properties since many decades now. The  $R^{\frac{1}{4}}$  law (de Vaucouleurs 1948) describing almost perfectly luminous early-type galaxy light profiles, and the exponential law (Freeman 1970) which instead well fits the light profile of disk-dominated galaxies, have been extensively used to derive galaxy physical quantities, such as the effective radius and surface brightness. This has in fact allowed to formulate and study galaxy scaling relations, such as the Tully–Fisher (Tully & Fisher 1977) or the Fundamental Plane (Dressler et al. 1987; Djorgovski & Davis 1987; Bender et al. 1992), which have enormously boosted our knowledge and understanding of galaxy evolution and formation.

The  $R^{\frac{1}{4}}$  and the exponential laws may be used in the same modeling to describe both the bulge and disk photometric components of a single galaxy (see, e.g., Simard et al. 1999). This approach is in fact doable only for very high signal-to-noise objects as the number of parameters involved becomes

fairly large and hence the fitting itself heavily degenerate. For this reason, the use of the more simple and robust single component Sérsic (1968) model has become very popular.<sup>9</sup> This is a convenient generalization of the  $R^{\frac{1}{4}}$  profile with  $R^{\frac{1}{n}}$ , where  $n$  is called the Sérsic index. The variation of the index  $n$  allows to describe very different galaxy light profiles from the classical  $R^{\frac{1}{4}}$  ( $n = 4$ ), to the late-type galaxy exponential profile ( $n = 1$ ), to the massive elliptical galaxy profiles ( $n \geq 3.5$ ) and down the unresolved point-like Gaussian profiles ( $n = 0.5$ ).

The Sérsic profile fitting, thanks to its flexibility and robustness, has become a preferred tool in the last years to classify galaxies in broad morphological classes (e.g., Shen et al. 2003; Trujillo et al. 2004; Ravindranath et al. 2004; Barden et al. 2005; McIntosh et al. 2005; Pannella et al. 2006; Häussler et al. 2007), possibly combined to the “bumpiness” parameter as done in Blakeslee et al. (2006) and van der Wel (2008).

The main idea behind the nonparametric approach is to measure model independent quantities, such as the concentration, the asymmetry (Abraham et al. 1996; Conselice 2003), the  $M_{20}$  and the Gini parameters (Abraham et al. 2003; Lotz et al. 2004; Scarlata et al. 2007a) of the galaxy light distribution and to correlate these quantities to the visual galaxy appearance. Albeit being model independent, and hence conceptually more effective in describing the variegated galaxy morphology zoo, these classification schemes are not free from severe biases as addressed in Blanton et al. (2003) and more recently in Lisker (2008).

Having in mind to continue the study presented in this paper by investigating also the evolution of galaxy sizes, we opted for the parametric approach, that delivers both morphological classifications and structural parameters.

In this context the Cosmic Evolution Survey (COSMOS; Scoville et al. 2007b) is the ultimate effort to cover a sensitive patch of the sky ( $2 \text{ deg}^2$ ) with *HST*, going factors of 10/100/1000 wider than previous efforts like the Hubble Deep Field-North (HDF-N; Williams et al. 1996), GEMS (Rix et al. 2004), the Great Observatories Origins Deep Survey (GOODS; Giavalisco et al. 2004), the FORS Deep Field (FDF; Heidt et al. 2003), among many others.

The high-resolution imaging has been complemented in COSMOS by a state-of-the-art multiwavelength coverage all the way from the X-ray to the radio. By observing the universe in all its colors COSMOS is becoming a real breakthrough in observational cosmology. The need to tackle and understand the conspiracies of nature embedded in the universe variance makes of this wide and deep survey a unique and unprecedented tool for galaxy evolution studies.

In this work, we rely on a deep and accurate ( $i \lesssim 26.5$  and  $\Delta z/(z_{\text{spec}} + 1) \approx 0.035$ ) photometric redshift catalog (Gabasch et al. 2008) complemented with a morphologically classified sample ( $F814 \lesssim 24$ ) to study the contribution of galaxies of different morphologies to the redshift evolution of the stellar mass density, as well as its dependence on the environmental density, over an area of  $\sim 0.7 \text{ deg}^2$  in the COSMOS field.

Brinchmann & Ellis (2000), Bundy et al. (2005), Pannella et al. (2006), and Franceschini et al. (2006) have carried out studies on the evolution of the galaxy stellar mass function split by morphological types, in a way qualitatively similar to the one we present here, but based either on shallower samples and visual morphological classification or on much smaller areas heavily affected by cosmic variance. Likely due

<sup>9</sup> We refer to Appendix A for the analytic expression of the Sérsic profile.

to the small surveyed area, no one of the just mentioned studies defined environmental properties of galaxies in order to contrast the effect of local environment against cosmic time on morphological evolution.

This paper is organized as follows: in Section 2 we discuss the ground-based data set and the photometric redshifts on which this work is based, in Section 3 we discuss how galaxy stellar masses have been estimated, in Section 4 we present the ACS data used in this work, the source extraction and the galaxy number counts, in Section 5 we briefly describe the quantitative morphological analysis, referring to a more detailed discussion in Appendix A, in Section 6 we present the evolution of the morphological mass function and mass density, in Section 7 we discuss the effect of local environments on galaxy morphological evolution, and finally in Section 8 we summarize our results and draw our conclusions.

Throughout this work, we use AB magnitudes and adopt a  $\Lambda$  cosmology with  $\Omega_M = 0.3$ ,  $\Omega_\Lambda = 0.7$ , and  $H_0 = 70 \text{ km s}^{-1} \text{ Mpc}^{-1}$ .

## 2. GROUND-BASED DATA AND PHOTOMETRIC REDSHIFTS

The ground-based data used in this paper combine the *uBVrizK* COSMOS data set<sup>10</sup> with proprietary imaging in the *H* band. A highly homogeneous multiwavelength *i*-band selected catalog is used to derive accurate photometric redshifts. A full description of the NIR data acquisition, data reduction and catalog assembling, and of the photometric redshifts estimation, is presented in Gabasch et al. (2008). Here, in the following, for the sake of clarity, we give only a brief summary.

Our *cleaned i*-selected catalog<sup>11</sup> comprises 293,377 objects over an area of  $\sim 0.7 \text{ deg}^2$  down to a limiting magnitude  $\sim 26.5$ . There is a good agreement between literature data and this catalog number counts up to the 25th magnitude. At the bright end ( $i \leq 21$ ), the literature number counts are sensibly higher since most of the very bright objects are saturated in the Subaru *i*-band images and thus not present in the final catalog. Since objects brighter than  $i = 21$  are likely to be important for the determination of the high-mass end of the galaxy stellar mass function at low and intermediate redshifts, we added those objects (1896) back to our catalog by complementing it with the COSMOS legacy photometric catalog described in Capak et al. (2007b), where Canada–France–Hawaii Telescope (CFHT) *i*-band photometry was used for this bright tail.

Photometric redshifts were derived using the technique described in Bender et al. (2001), Gabasch et al. (2004a), and Brimiouille et al. (2008). In short, the method consists of: (1) checking photometric zero points and, if necessary, determining photometric offsets by comparing theoretical and observed stellar *locii*; (2) computing object fluxes in a fixed aperture ( $2''.0$ ) from seeing-matched images; and (3) determining a redshift probability function  $P(z)$  for each object by matching the object's fluxes against a set of template spectra covering a wide range of stellar population ages and star formation histories (SFHs).

The additional use of the *Galaxy Evolution Explorer* (GALEX) FUV and NUV bands (Zamojski et al. 2007) allowed some photo-*z* degeneracies to be broken, and a final accuracy of  $\Delta z / (z_{\text{spec}} + 1) \approx 0.035$  to be reached. Figure 1 shows the

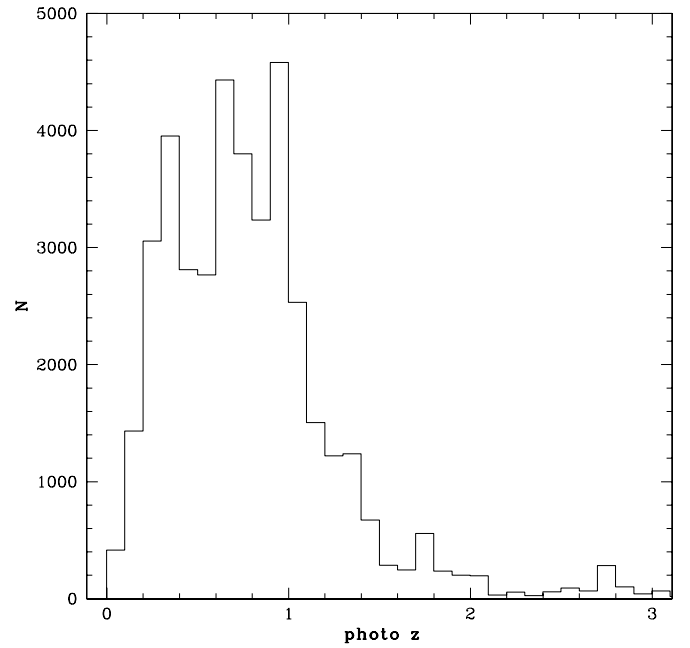


**Figure 1.** Redshift distribution of the 41,300 galaxies belonging to the morphological catalog used in the present work. Overdensities at redshifts 0.4, 0.7, and 1 are quite prominent, as well as the underdensities at redshifts 0.5 and 0.8.

redshift distribution of the subsample with available morphological information used in this work.<sup>12</sup>

The morphological catalog, including stellar mass estimates, analyzed in this work is made publicly available at the following Web site: <http://www.aoc.nrao.edu/~mpannell/data.html>.

## 3. COMPUTING MASS-TO-LIGHT RATIOS

The method we use to infer stellar masses from multiwavelength photometry is described in detail in Drory et al. (2004a). It is based on the comparison of the observed multicolor photometry with a grid of stellar population synthesis models produced with the Bruzual & Charlot (2003) code.

We parameterize the possible SFHs by a two-components model, consisting of a main, smooth component described by an exponentially declining SFR  $\psi(t) \propto \exp(-t/\tau)$ , linearly combined with a secondary burst of star formation. The main component timescale  $\tau$  varies in  $\in (0.1, \infty)$  Gyr, and its metallicity is fixed to the solar metallicity. The age of the main component,  $t$ , is allowed to vary between 0.5 Gyr and the age of the universe at the object's redshift.

The secondary burst of star formation is modeled as a 100 Myr old constant SFR episode of solar metallicity.

We adopt a Salpeter (1955) initial mass function (IMF) for both components, with lower and upper mass cutoffs of 0.1 and  $100 M_\odot$ .

Additionally, adopting the Calzetti et al. (1994) extinction, both the main component and the burst are allowed to exhibit a variable amount of attenuation by dust with  $A_V^{1,2} \in (0, 1.5)$  and  $(0, 2)$  for the main component and the burst, respectively. This takes into account the fact that young stars are found in dusty environments and that the starlight from the galaxy as a whole

<sup>10</sup> Publicly available at <http://irsa.ipac.caltech.edu/data/COSMOS>.

<sup>11</sup> Publicly available at <http://www.mpe.mpg.de/~gabasch/COSMOS>.

<sup>12</sup> In the last stages of this work the COSMOS Legacy released a new catalog of spectroscopic redshifts within the zCOSMOS DR2 (Lilly et al. 2007) as well as an updated catalog of photometric redshifts (Ilbert et al. 2009a). We refer to Appendix B for a comparison with these two catalogs.

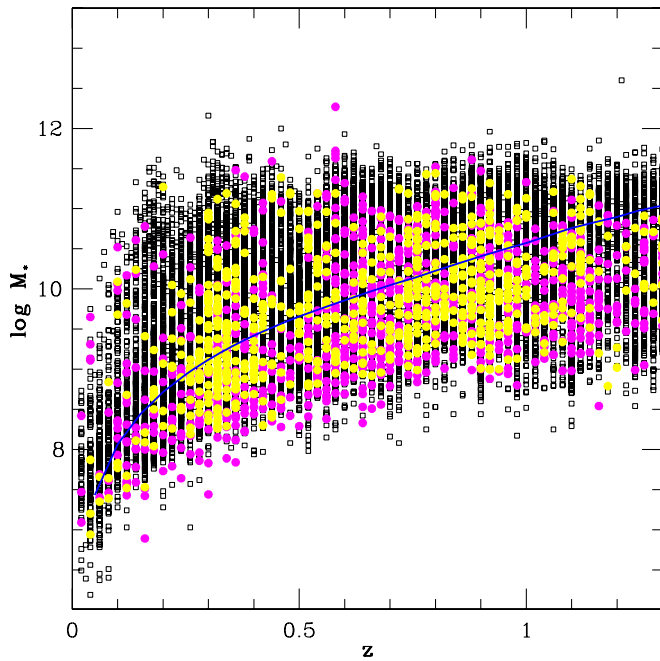


**Figure 2.** Distribution of galaxy stellar masses, derived using a Salpeter (1955) IMF, as a function of redshift for the morphological catalog used in this work (empty squares). The solid blue line shows the estimated mass completeness of the morphological sample at each redshift (see the text for details). For comparison, data from the morphological catalog used in Pannella et al. (2006) are overplotted (yellow and magenta symbols for the FDF and GOODS-S fields, respectively).

may be reddened by a (geometry dependent) different amount. We compare this set of models with multicolor photometry of each object, computing the full likelihood distribution in the five-dimensional parameter space ( $\tau$ ,  $t$ ,  $A_V^1$ ,  $\beta$ ,  $A_V^2$ ), the likelihood of each model being  $\propto \exp(-\chi^2/2)$ .

To compute the likelihood distribution of mass-to-light ratios  $M/L$ , we weight the  $M/L$  of each model by its likelihood and marginalize over all parameters. The uncertainty in  $M/L$  is obtained from the width of this distribution.

For young objects, with relatively high burst fractions, the width of the  $M/L$  distribution is usually much wider in the optical than in NIR bands, while for quiescent objects the width of the  $M/L$  distribution is very similar in all bands. On average, the width of the likelihood distribution of  $M/L$  at 68% confidence level is between  $\pm 0.1$  and  $\pm 0.2$  dex (using the  $B$ -band  $M/L$ ). The uncertainty in mass has a weak dependence on mass itself (increasing with lower signal-to-noise ratio (S/N) photometry), and it mostly depends on the spectral type: quiescent galaxies have more tightly constrained masses than star-forming ones.

We estimated the galaxy stellar masses for all the objects in the  $i$ -band selected catalog down to the limiting magnitude.

In Figure 2 we show the distribution of galaxy stellar masses as a function of redshift for the morphological catalog used in this work. For comparison, and to show the impressive statistic available, we overplot the morphological catalogs used in Pannella et al. (2006) from the FDF (yellow) and GOODS-S (magenta) fields.

In Figure 3 we show the stellar mass density up to redshift 1 for objects with  $\log M_* \gtrsim 10.8$ , which corresponds to the mass completeness value for the highest redshift considered. The dashed lines represent  $1\sigma$  estimates of the local mass density from Bell et al. (2003) after applying the same mass cut.

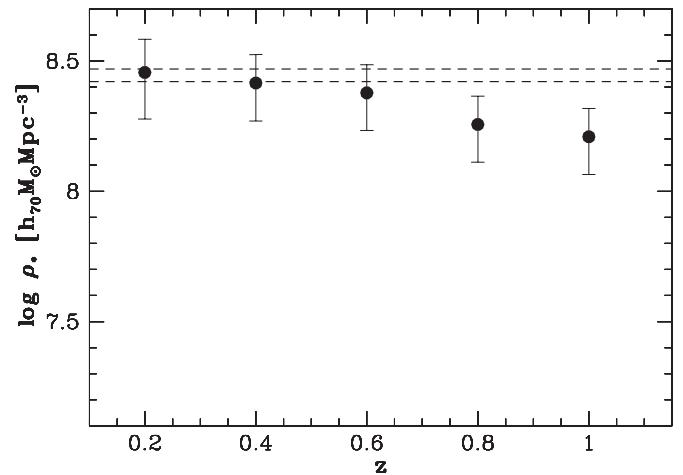


**Figure 3.** Cosmic stellar mass density up to redshift 1 for objects with  $\log M_* \gtrsim 10.8$ , corresponding to the mass completeness value for the highest redshift considered. The horizontal dashed lines show the local mass density from Bell et al. (2003) after correcting for the different IMF and applying the same mass cut. The error bars represent the cosmic variance contribution (Somerville et al. 2004). Assuming that the mass function evolves only in normalization over this redshift range, adding 0.28 dex to the plotted values gives the total mass densities.

**Table 1**  
log  $M_*/M_\odot$  Completeness versus Redshift

$z$	0.25	0.45	0.65	0.85	1.05	1.25
F814W (24)	8.9	9.4	10.0	10.3	10.7	11
$i$ (26)	8.2	8.8	9.2	9.6	10.0	10.3

The error bars represent the cosmic variance contribution, as estimated in Somerville et al. (2004), that is a factor of 10 larger than statistical errors. Assuming that the mass function evolves only in normalization over this redshift range, one should add 0.28 dex to the plotted values to recover the total mass densities.

The mass completeness at different redshifts was estimated as the mass of a maximally old stellar population<sup>13</sup> having, at the redshift considered, an observed magnitude equal to the catalog completeness magnitude (e.g., Dickinson et al. 2003). In Table 1 we provide the mass completeness values as a function of redshift for the morphological catalog (F814W < 24), as well as for the global photometric catalog ( $i < 26$ ).

#### 4. HST ACS IMAGING

The 2 deg<sup>2</sup> COSMOS field was imaged in the F814W ACS filter for a total of 581 orbits. Within each orbit, four equal length exposures of 507 s duration each (2028 s total) were obtained in a four position dither pattern, designed to shift bad pixels and to fill in the 90 pixel gap between the two ACS CCD arrays. Adjacent pointings in the mosaic were positioned with approximately 4% overlap in order to provide at least three exposure coverage at the edge of each pointing and four exposure coverage over approximately 95% of the survey area. This multiple exposure coverage with ACS provided excellent cosmic ray rejection.

A full description of the ACS data processing including drizzling, flux calibration, registration, and mosaicing is provided in Koekemoer et al. (2007) and Scoville et al. (2007a).

<sup>13</sup> We used a dust-free, passively evolving stellar population model, ignited by an instantaneous burst of subsolar ( $Z = 0.008$ ) metallicity at  $z = 10$ .

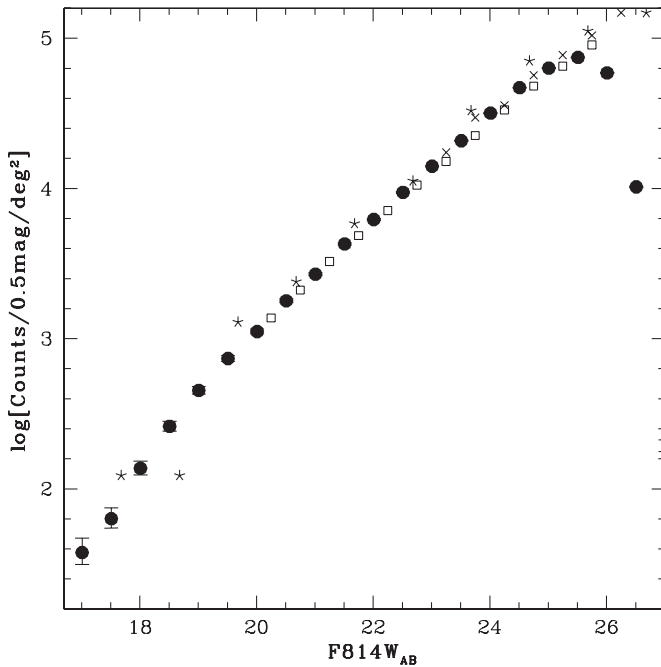


**Figure 4.** Galaxy number counts for the ACS/F814W passband are plotted as solid dots. The error bars account for Poissonian errors only, and no correction for incompleteness has been applied. Literature data are plotted with other symbols and are taken from Pannella et al. (2006; asterisks, FDF), Leauthaud et al. (2007) (open squares, COSMOS), and Benítez et al. (2004; diagonal crosses, VV 29).

The ACS images released to the public<sup>14</sup> are sampled with  $0''.05$  pixels. The measured full width at half-maximum (FWHM) of the point-spread function (PSF) in the ACS F814W band filter is  $\approx 0''.11$ .

#### 4.1. Source Extraction, Star–Galaxy Classification, and Cataloging

Source extraction was performed with the SExtractor code (Bertin & Arnouts 1996) on each ACS tile in a *cold* manner, in order to minimize the artificial source splitting and maximize the number of pixels assigned to each object.

We used 348 ACS tiles, namely, only those overlapping with the ground-based photometry used in this work.

Taking advantage of the ACS high-resolution imaging we could remove the point-like (stellar) objects using the structural parameters output by SExtractor. We used the FWHM, the half-light radius, the neural network stellarity index, and the total magnitude for each object to select point-like sources.

In Figure 4 we show F814W band galaxy number counts, not corrected for incompleteness, compared with literature counts (Pannella et al. 2006; Leauthaud et al. 2007; Benítez et al. 2004), and in Table 2 we provide the plotted values. The ACS galaxy catalog has been cross-correlated with the ground-based catalog with a 1 arcsec matching radius. We removed from the final catalog all the objects, a few percent of the total, for which one ground-based entry had more than one entry in the ACS catalog. The final morphological catalog used in the following contains 41,300 objects over  $\sim 0.7 \text{ deg}^2$  and results to be more than 90% complete down to  $F814W = 24$ .

**Table 2**  
Galaxy Number Counts not Corrected for Incompleteness in the F814W Passband ( $\sim 0.7 \text{ deg}^2$ )

F814W		
Mag	$\log N$	$\sigma_{\log N}$
17.01	1.576	0.0969
17.51	1.801	0.0728
18.01	2.137	0.0481
18.51	2.416	0.0343
19.01	2.655	0.0258
19.51	2.867	0.0201
20.01	3.047	0.0163
20.51	3.252	0.0128
21.01	3.429	0.0104
21.51	3.63	0.0082
22.01	3.793	0.0068
22.51	3.974	0.0055
23.01	4.148	0.0045
23.51	4.318	0.0037
24.01	4.501	0.0030
24.51	4.671	0.0025
25.01	4.802	0.0021
25.51	4.872	0.0020
26.01	4.769	0.0022
26.51	4.01	0.0053

**Note.**  $\log N$  and  $\sigma_{\log N}$  are given, where  $N$  is in units of  $0.5 \text{ mag}^{-1} \text{ deg}^{-2}$ .

## 5. THE MORPHOLOGICAL ANALYSIS

We use the package GIM2D (Simard et al. 1999) to fit PSF convolved Sérsic (1968) profiles to the two-dimensional surface brightness distribution of each object, for all sources down to a limit of  $F814W = 24$ . The PSFs used to convolve the profiles were obtained for each individual tile by median stacking about 50 high S/N stars.

We tested our results by running also the GALFIT (Peng et al. 2002) code on some of the COSMOS ACS patches. The results from the two different codes are in excellent agreement, thus confirming both the robustness of our modeling and the choice of flux limits.

We further tested our results by running the GIM2D code on simulated images. This test was performed by adding to the real image, in a blank, pure-sky region, fake objects with Sérsic profiles, and structural parameters spanning a wide range of plausible values. The whole procedure is then run exactly as for real objects: we find that the profile parameters of simulated objects are well recovered down to  $F814W = 24$ . High Sérsic index objects have very extended wings that, depending on the total flux, can fall under the sky surface brightness, thus for these objects a lower Sérsic index, the total flux and effective radii are usually recovered (see also Sargent et al. 2007). We point out that the same trend was found in Trujillo et al. (2006b) with a different fitting code, thus confirming the “physical bias” as contrasted to a code failure. In the local universe a tight correlation between Sérsic index and luminosity/mass of giant elliptical galaxies (see, e.g., Caon et al. 1993; Graham et al. 2001) has been robustly established. Due to flux limits and mass completeness, morphological analysis of high redshift ellipticals is mostly limited to the most massive galaxies which one would expect to have relatively high Sérsic index. Our simulations show that for such high Sérsic index objects at faint apparent magnitudes (low S/N) we would recover Sérsic indices and effective radii biased toward

<sup>14</sup> Publicly available at <http://irsa.ipac.caltech.edu/data/COSMOS/>.

lower values. While we will deal in detail with the galaxy size evolution in a future work, we argue here that the strong size evolution of early-type galaxies with redshift, recently reported in the literature (e.g., Trujillo et al. 2006a; Cimatti et al. 2008; van Dokkum et al. 2008), could be partly due to such bias. We try to cope with this “biased” Sérsic index by adopting the procedure described in the following. We perform extensive Monte Carlo simulations to take into account the Sérsic index uncertainty ( $\approx 30\%$ , estimated through simulations) on our results. One thousand simulations of the morphological catalog were generated. Objects with Sérsic index smaller than 2.5 were perturbed within a Gaussian of sigma equal to the 30% of the measured value. Objects with Sérsic index larger than 2.5 were perturbed within only the positive side of the Gaussian so that their value could only get larger than the measured ones. We tried also to implement different solutions to this correction procedure and the final results were always in good agreement. More details on the morphological analysis are given in Appendix A.

## 6. THE EVOLUTION OF THE GALAXY STELLAR MASS FUNCTION BY DIFFERENT MORPHOLOGIES

Pannella et al. (2006) show that there is a good correlation between the average visual and automated classifications as parameterized by the morphological type  $T$ , assigned according to the de Vaucouleurs et al. (1991) classification scheme, and the Sérsic index  $n_{\text{ser}}$ , respectively (see Figure 1 in that paper). Following Pannella et al. (2006), we split our sample, according to the Sérsic index value in three broad morphological classes: early type ( $n \geq 3.5$ , which corresponds to bulge-dominated/elliptical galaxies), intermediate ( $2 \leq n < 3.5$ ), and late type ( $n < 2$ , which corresponds to disk-dominated galaxies).

We restrict our analysis to  $z \leq 1.2$  to limit the bias introduced by the rest-frame emission band shifting, namely, the effect of the morphological  $k$ -correction. A number of studies in the last years have shown, although not in a conclusive and quantitative way, that this is indeed a fair assumption (e.g., Scarlata et al. 2007b; Abraham et al. 2007).

We performed extensive Monte Carlo simulations to take into account the effect of mass uncertainties ( $\approx 0.2$  dex) on our results. One thousand simulations of the mass catalog were generated, perturbing each mass within a Gaussian of sigma equal to its error. Unless stated differently in the relevant figure captions, we use the median values of the Monte Carlo simulations in all figures. The error bars take into account both Poissonian errors on the median counts (Gehrels 1986), and 16–84th percentile values of each distribution.

In Figure 5 we show the  $V/V_{\text{max}}$  corrected number density evolution split by morphological type, up to redshift 1.2, for objects in stellar mass ranges  $\log M_* = (10.6\text{--}10.8)$ ,  $(10.8\text{--}11)$ ,  $(11\text{--}11.2)$ , and  $(11.2\text{--}12)$ , as indicated in the upper right corner of each panel. By multiplying the number densities by the average mass in the corresponding mass range, each panel can be interpreted as the evolution of the total mass densities contributed by objects in that stellar mass range. The dotted vertical lines show the estimated redshift completeness for the relevant mass bin.

We find that early-type objects always dominate the high-mass end. The lower the stellar mass, the more late-type objects tend to dominate the relative contribution to the total number/mass density. The same trend is true by looking at increasing redshift: the higher the redshift the more the relative contribution of early and late types gets closer. For the lowest mass range

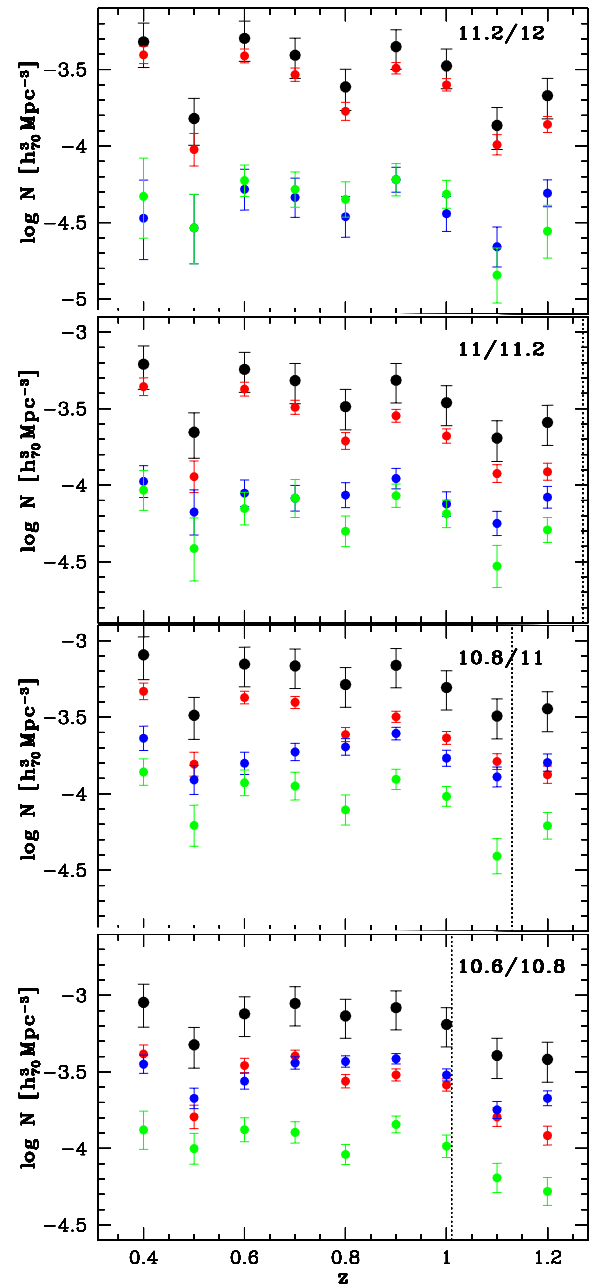


**Figure 5.** Number densities as a function of redshift and morphology. The panels show the number density for different stellar mass bins, as indicated in units of  $\log(\text{stellar mass})$  in the upper right corner of each panel. The vertical dotted lines show the limiting redshift for which the sample in the considered stellar mass bin is complete. Symbols are colored according to the morphological split (black, total; red, early; green, intermediate; blue, late).

$(10.6\text{--}10.8)$  the transition from a bulge-dominated to a disk-dominated stellar mass budget happens around redshift 0.7; beyond that redshift late types are always contributing more to the total mass budget. In the mass range  $\log M_* = (10.8\text{--}11)$  the transition is occurring at  $z \approx 1.1$ .

At each redshift, a *transition mass* can be identified where the transition from a bulge-dominated to a disk-dominated stellar mass budget takes place. Based on the very good statistics available in this work, we are able to confirm the main conclusions of Pannella et al. (2006): (1) the morphological mix at the high-mass end evolves with redshift and (2) the transition mass increases with redshift. At  $z \sim 0.7$  we find a

value of the transition mass approximately consistent with the local value  $M \approx 5 \times 10^{10} M_{\odot}$ , as measured in Bell et al. (2003) by using the concentration parameter to discriminate between early- and late-type objects in a complete sample extracted from local surveys. At  $z \sim 1$  the late- and early-types contributions become comparable at  $M \approx 1 \times 10^{11} M_{\odot}$ .

In a fixed mass range the number densities of late types are consistent with being constant with redshift, while the early types follow the more general total declining. At a fixed redshift, the number density of early types of different masses is very similar (in  $\pm 0.1/0.2$  dex), while the late-type number densities move by 1 order of magnitude passing from the high to the low stellar mass range. This naturally sets the evolution of the transition mass with redshift.

The slope of the redshift evolution of total number densities is consistent in all mass ranges, at least up to the common redshift completeness, meaning that the mass function in its high-mass end, i.e., at least down to  $M \approx 4 \times 10^{10} M_{\odot}$ , does not evolve in shape but only in normalization with redshift.

## 7. DISENTANGLING THE ROLE OF ENVIRONMENT ON GALAXY MORPHOLOGICAL EVOLUTION

In Figure 5 there is obvious scatter around the mean number density decline in all the mass bins. However, an underdensity at  $z \sim 0.5$  shows up quite strikingly. The deficit of objects is also quite evident in the global redshift distribution of our morphological catalog, as shown in Figure 1. It gets more and more significant with increasing stellar mass. The deficit of galaxies at this redshift is a factor of 3 for the highest mass objects, and less than a factor of 2 for objects in the lowest mass bin explored. This differential deficit is in qualitative agreement with galaxy evolution dependence on the local density as expected in current galaxy formation models (see Lee 2006, and references therein): the more underdense is the environment the later massive objects will assemble because there is in general a time delay in starting star formation and also there are less small galaxy units to assemble the massive giant galaxies.

From the morphological point of view, the evolution in this underdense redshift bin is *delayed* at all stellar masses as compared with the contiguous redshift bins. The early-type fraction with respect to both the total number density and the late-type number density is much lower than those in the contiguous redshift bins, in agreement with the expectations from the morphology–density relation. We also note that in the highest mass bin, in this underdense region there are no massive late-type galaxies.

We note that the morphological mix in this underdense redshift bin is, at all masses probed, very close to the morphological mix at  $z \approx 1.1$ , which has a comparable total number density of objects.

Taking advantage of the good statistics available in this study, we wish to further check the importance and role of environment on galaxy morphological evolution.

Estimating the local volume density in a photometric redshift survey is not straightforward, and we try here to make it as simple and unbiased as possible.

First of all one has to decide which are the objects tracing the overdensities in a way not biased by the flux-limited survey: a density-defining population (DDP; Croton et al. 2005) of galaxies is needed. The objects have to be bright enough to be seen in the whole redshift range considered. Dealing with masses and morphologies, one should also take care of the selection effects introduced by the different  $M/L$  ratios

associated with different stellar populations. Basically, old stellar populations, which more often but not always reside in bulges, have much higher  $M/L$  ratios with respect to young stellar populations, often but not always populating disks. A pure luminosity cut—even taking into account passive evolution—would thus preferentially cut out of the sample high  $M/L$  objects (early types) with respect to low  $M/L$  objects (late types). To avoid this kind of bias, we use as DDP all objects with masses down to the mass completeness value at the highest redshift we are exploring ( $7 \times 10^{10}$  solar masses).

Another issue is the relative scarcity of these objects (being in the exponential cutoff of the mass function), so one has to avoid reaching the shot noise regime when calculating number densities.

With this in mind, we proceed as follows: we first fit the number density evolution with redshift for objects more massive than  $7 \times 10^{10}$  solar masses, obtaining in this way an expected value of the number density,  $\bar{\rho}(z)$ , at each redshift  $z$ . We then split the entire redshift range in slices of  $\Delta z = 0.1$  (corresponding to differential depths of about 327 comoving Mpc at redshift 0.5 and 244 at redshift 1). This slicing along the redshift axis turns out to be quite robust against the photo- $z$  errors, in fact this corresponds to about two times the formal photo- $z$  error at redshift 0.5 and 1.5 times at redshift 1. We then split the entire survey volume in cells of 2.8 comoving Mpc by side at each redshift slice, which is the maximum contiguous angular area we have available in the lowest redshift bin. Finally, we calculate the comoving number density of each cell at the different redshifts and assign the cell galaxy population to one of three density classes: underdense ( $\rho(z) \leq 0.5 \times \bar{\rho}(z)$ ), medium-dense ( $0.5 \times \bar{\rho}(z) < \rho(z) \leq 1.4 \times \bar{\rho}(z)$ ), and overdense ( $\rho(z) > 1.4 \times \bar{\rho}(z)$ ). The limits used here to define environmental classes are chosen to balance the needs to map sensibly different environments and to assign a relatively large number of objects to each of the three classes.

In Figure 6, we show the number density evolution for objects with  $\log M_* \gtrsim 10.8$ . The solid line,  $\bar{\rho}(z) = -2.62 - 0.36 \times z$ , shows the linear fit to the filled dots (i.e., the number densities obtained over the whole field in redshift bins of  $\Delta z = 0.2$ ). The dashed line sets the  $1.4 \times \bar{\rho}(z)$  limit above which we select the overdense regions. Below the dashed-dot line ( $0.5 \times \bar{\rho}(z)$ ) we select the underdense regions, while in between the two lines we select the medium-dense regions. The empty squares overplotted show the number densities in all the cells we have split our survey volume.

We run 100 realizations of the procedure adopted to define environmental densities by randomizing the initial position of the grid in the sky and also by adopting different solutions for the redshift slicing of the total volume. The outcome of this testing convinced us that the results we are going to show and discuss in the following are robust and not biased against the specific procedure.

### 7.1. Morphological Evolution and Mass Growth of Early- and Late-type Galaxies in $0.25 < z < 1.15$

In Figure 7 we show the galaxy stellar mass function as a function of redshift, split by morphology and for the different environmental densities as defined in the previous section. Each of the panels contains about 2000 objects. The vertical dotted lines set the estimated mass completeness at the different redshifts. For reference in all panels are overplotted local estimates for the stellar mass function (Cole et al. 2001; Bell et al. 2003), which are fixed and independent from the

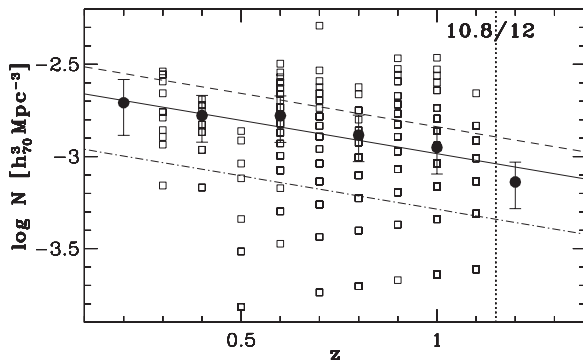


**Figure 6.** Number density evolution for objects with  $\log M_* \gtrsim 10.8$ . The solid line,  $\bar{\rho}(z) = -2.62 - 0.36 \times z$ , shows the linear fit to the filled dots (i.e., the number densities obtained over the whole field in redshift bins of  $\Delta z = 0.2$ ). The dashed line sets the  $1.4 \times \bar{\rho}(z)$  limit above which we select the overdense regions. Below the dashed-dot ( $0.5 \times \bar{\rho}(z)$ ) line we select the underdense regions, while in between the two lines we select the medium-dense regions. The empty squares overlotted show the number densities in all the cells we have split our survey volume.

environment. They are only meant as a reference to look at differential evolution in different environments.

In the lowest range explored, at  $z \sim 0.4$ , the mass completeness reaches masses as low as  $7 \times 10^9 M_\odot$ . This enables us to explore the behavior of the slope of the mass function in different environments. The slope of the mass function is marginally evolving from the lower to the higher density regions, becoming increasingly shallower and consistent with the local *field* one. This trend is in fact in good agreement with what found in the local universe (Baldry et al. 2006).

The transition mass moves from  $\log M_* \simeq 10.6$  at high density to  $\log M_* \simeq 10.9$  at low density.

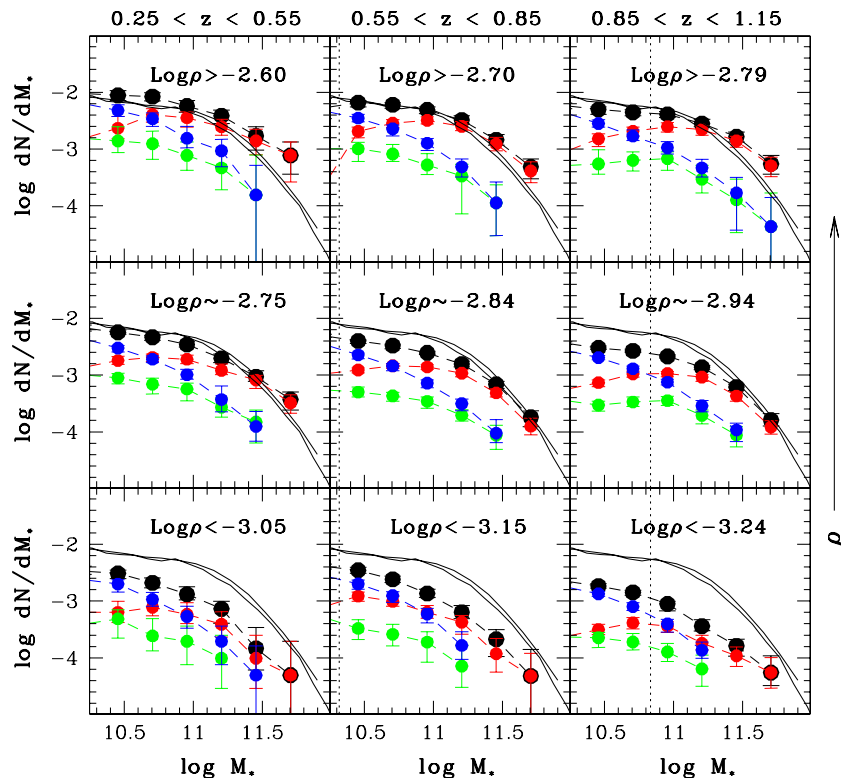
In the overdense and medium-dense environments, the shape of the mass function is in a very good agreement with the local determinations. In the overdense regions, this happening at all redshifts, a very massive bulge-dominated population seem to appear that overcomes the local *field* determination.

Figure 7 shows that the morphologically split mass function evolves along both the redshift and the density axes. The evolution is differential though: the redshift evolution is much milder than the environmental one.

This is in fact a crucial point in interpreting the results since in almost all previous studies there has been no chance to split these two very different contributions. This is better explained by the following examples: the total mass function, and the morphological mixtures are basically the same, up to the common mass completeness value, for overdense volumes at redshift 1 and medium-dense volumes at redshift 0.4. The transition mass is close to  $\log M_* = 11$  at redshift 1 in medium-dense volumes and it is already at that mass in the underdense environments at  $z \sim 0.4$ . This shows how by analyzing small patches of the sky one could mix up different environments at different redshifts and hence get the wrong evolutionary paths for different morphologies.

With the aim of trying to better quantify the morphological mix evolution as a function of redshift and environment, we integrate the mass function over the common complete mass range in the three redshift bins and in the three different environments.

In Figure 8, we show both the early-type fraction (lower panel) and the early- to late-type classification ratio (upper panel) at



**Figure 7.** Galaxy stellar mass functions as a function of redshift, morphology, and local environment. Black symbols refer to the total values. The vertical axis is in units of  $(h_{70}^3 \text{ Mpc}^{-3} \text{ dex}^{-1})$ . A vertical dotted line indicates the mass completeness limit in each redshift bin. Colored symbols refer to morphological classes, see Figure 5 for details. The dashed colored lines are only intended to guide the eye. The solid black lines show the local *field* mass function determinations from Cole et al. (2001) and Bell et al. (2003).

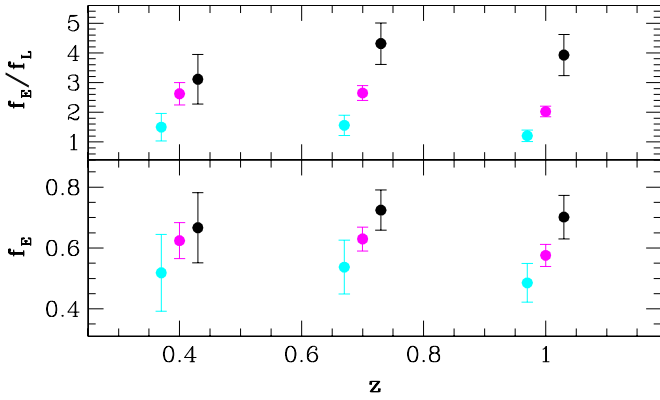


**Figure 8.** Morphology–density relation at work. The bottom panel shows the early-type fraction as function of redshift and environment. The environment is color coded as: black, high; magenta, medium; cyan, low. The upper panel shows the early- to late-type classification ratio for different redshift and different environments. All the fractions are computed for objects more massive than  $\log M_* > 10.8$ .

(A color version of this figure is available in the online journal.)

different redshifts and for different environments (low, cyan; medium, magenta; black, high density).

At all redshifts a morphology–density relation, as already reported in the literature (e.g., Smith et al. 2005), is showing up: denser volumes contain also a higher relative fraction of bulge-dominated galaxies with respect to lower density volumes. Although it is difficult to compare with previous results given the fact that in our study for the first time, to our knowledge, a mass complete sample has been adopted, it is very reassuring that qualitatively we are in agreement with previous studies. This confirms the robustness of our galaxy environment definition procedure.

As a function of redshift, in the medium- and low-density environments there is an increase of the early-type population with cosmic time which is more pronounced between redshift 1 and 0.7 and then flattens out to redshift 0.4. In the high-density environments the early-type fraction grows between redshift 1 and 0.7, and then seems to turn-over to redshift 0.4. A similar behavior has been actually found in Capak et al. (2007a). In our opinion the sky patch, we are using here, might not cover enough cosmic volume at redshift around 0.4 to allow an exact environmental definition. This shows up in Figure 6 where all but two subvolumes are in fact assigned to the medium-density environment bin.

## 7.2. The Ages of Early Types in Different Environments

In Figure 9, we show the ages of massive early-type galaxies as a function of redshift and for different environments as obtained from the spectral energy distribution (SED) fitting procedure outlined above. The redshift ranges considered are indicated in the top label of each panel. We cut the total sample to the common completeness limit ( $\geq 7 \times 10^{10} M_\odot$ ). The dotted, dashed, and solid histograms represent the high-, medium-, and low-density environments, respectively. In each panel, the difference in billion years between the mean ages in the two most extreme environments (the high- and low-density regions) is indicated. Such differences deviate from zero at a two sigma level at all redshifts, and might suggest an earlier formation epoch of early-type galaxies in high-density environments with respect to those living in a low-density region. The results found are in good agreement with recent studies (e.g., Thomas et al. 2005; van Dokkum & van der Marel 2007; Gobat et al. 2008; Rettura et al. 2008).

From Figure 9 three things are worth noting: first, the histograms are quite similar to each other within each single panel (as confirmed by a Kolmogorov–Smirnov test) but for the oldest and youngest tails of the distribution which preferentially belong to the highest and the lowest density regions; second, the width of the distributions is increasing with the cosmic clock, this being partially driven by the narrower range of ages allowed at earlier cosmic times; third, in the lowest redshift bin a number of, relatively young, early-type objects are present which cannot be the descendants of the higher redshifts early-type populations simply evolved by passive evolution.

We interpret these evidences as follows: (1) young massive early-type galaxies are preferentially found in low-density environments at all redshifts; (2) the bulk of the early-type stellar populations have similar characteristic ages independent of the environment; (3) the oldest objects in the universe, or better saying the oldest stars in the universe, happen to belong to its highest density regions; and (4) newly formed, or somehow rejuvenated, bulge-dominated galaxies are entering the sample with cosmic time. This latter finding might explain why the difference in age seems to increase with the cosmic clock and reach the 2 Gyr quoted by Thomas et al. (2005) in the local universe.

The estimate of stellar population ages suffers from some important degeneracies and has to be treated with a *pinch of salt*. The SED modeling we have described in Section 3 only considers stellar population models with solar metallicity.

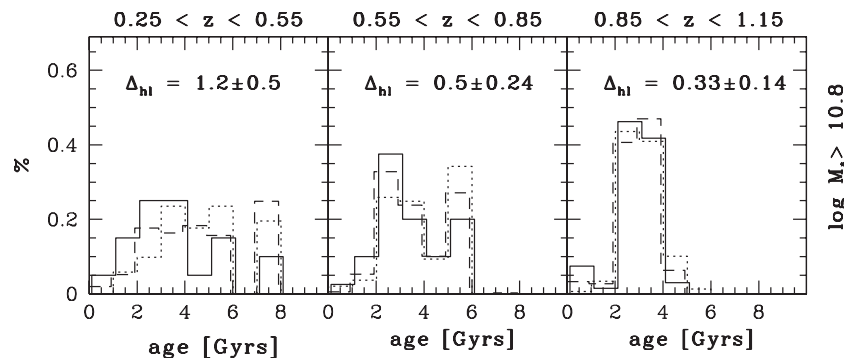


**Figure 9.** Ages of massive ( $\geq 7 \times 10^{10} M_\odot$ ) early-type objects at different redshift and for different environments. The difference, in billion years, between the mean ages of early-type galaxies in high- and low-density environment is indicated in each panel. The dotted, dashed, and solid histograms represent the high-, intermediate-, and low-density environments, respectively.

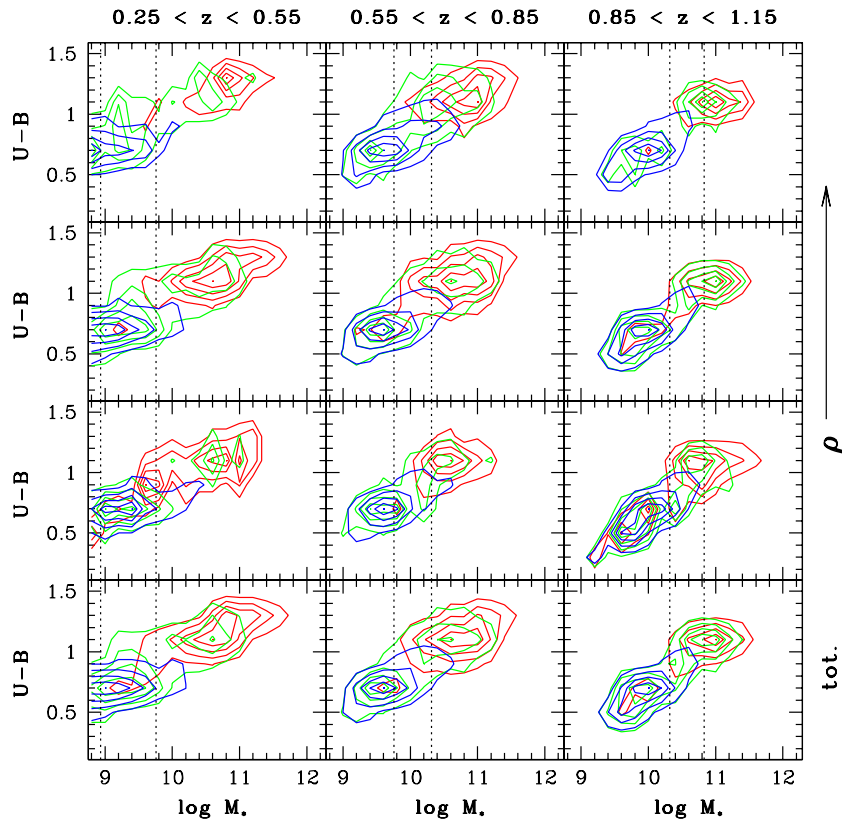


**Figure 10.**  $U - B$  rest-frame color as a function of mass, redshift, morphology, and environment. The color coding is according to the morphological classes (red, early; green, intermediate; blue, late). The bottom row shows the total values, i.e., the first three rows, from the top, collapsed. Contours define the morphological classes and are drawn as explained in the text. The two dotted lines show the estimated mass completeness values of our sample at the upper and lower edges of each redshift bin.

This means we are not tackling the well known age–metallicity degeneracy: old stellar populations with low metallicities and younger stellar populations with high metallicities may well have very similar SEDs. Only recently Cooper et al. (2008), but see also Mouhcine et al. (2007) for different conclusions, reported on a mild observed correlation between metallicity and environment: massive galaxies in high-density environments are slightly more metal rich than galaxies belonging to low-density environments. If such a correlation is indeed at work our results are biased and the correct differences in age would be even smaller than the ones reported in the panels of Figure 9.

We remind that our classification scheme does not allow any separation between ellipticals and early-type spirals. Therefore, as happens in the local universe (see, e.g., Dressler 1980) our early-type samples will be likely dominated by elliptical and S0 galaxies in overdense environments and by early-type spirals in low-density regions.

### 7.3. Red Sequence and Blue Cloud

In Figure 10 we show the rest-frame  $U - B$  color as a function of mass, redshift, morphology, and environment. Morphological classification is highlighted in different colors (red, early; green, intermediate; blue, late).

Contours are used to better show the different behavior of the three morphological classes. The contours correspond to equally spaced levels between the minimum and maximum density of the data points of each morphological set. The first three rows of panels starting from the top, show the high-, medium-, and low-density environments. The bottom row shows instead the total

population, i.e., all the different environments together. Redshift ranges are indicated, for each column, in the top label.

The red sequence, mostly populated by early types, in all environments becomes slightly redder with cosmic time because of the ageing of the stellar populations. The evolution in the rest-frame  $U - B$  color is mild, as also shown for instance by Willmer et al. (2006) up to  $z \approx 1.3$ . The red-sequence upper envelope reddens by  $\Delta(U - B) \approx 0.25$  mag in the redshift range  $0.25 < z < 1.15$ , in agreement with simple passive evolution expectations.

The bulge-dominated galaxy population is mostly confined to the red sequence with some peculiarities dependent on environments. At all redshifts, in higher density environments early types tend to be more confined to the massive end of the red sequence. On the other hand, in lower density environments early types tend to populate the red sequence down to lower masses (as it is easier to see at low redshifts) and reach into the blue cloud. This definitely points toward a difference in age between the bulge-dominated populations in different environments.

It is worth noting the evolution of the intermediate-type population: these are mainly spiral galaxies hosting fairly massive central bulges. At redshift 1, intermediate-type galaxies overlap in the color–mass diagram with both the early and late populations in all environments. As time goes by, this class of objects tend to leave the very high-mass end of the red sequence in favor of bulge-dominated galaxies, and to drift toward the bluer late-type population. This suggests that part of these intermediate-type galaxies have moved to the early-type population. The change of this class of objects with cosmic

time correlates with the environmental density: at low redshifts, intermediate-type objects in more dense environments tend to occupy the *valley* between the red sequence and the blue cloud, while in low-density environments they split in two populations, with the majority well overlapping the late-type population, and a minor subpopulation remaining in red sequence together with the massive bulge-dominated galaxies.

The late-type population is confined at all redshifts and in all environments to the blue cloud. Given the mass completeness limits it is definitely hard to make strong conclusions, but these data suggest the presence, possibly more pronounced at higher redshift and in lower density environments, of a population of massive disk-dominated galaxies reaching toward the red sequence.

In Section 7.1, we have investigated the evolution with redshift of the morphology–density relation (see Figure 8). Since Figure 10 shows that at all redshifts early types populate mainly the red sequence while late-type galaxies are mostly in the blue cloud, we can infer from our data that a color–density relation is in place up to the highest redshift explored.

Cucciati et al. (2006) analyzed a sample of 2900 galaxies with secure spectroscopic redshift determinations drawn from the VIMOS-VLT Deep Survey (VVDS; Le Fèvre et al. 2005) in an area four times smaller than the one considered in this work and with  $\approx 32\%$  sampling, slightly biased toward faint objects, of the whole galaxy population. They obtain a very similar result to the one we present in this work up to redshift 1.2, while claiming a dramatic evolution in the redshift bin 1.2–1.5 with blue star-forming galaxies belonging preferentially to the highest density environments. Since they define environmental properties based on a volume-limited sample, i.e., an absolute magnitude cut at all redshifts, which is biased against old stellar populations, it would be interesting to check whether this effect persists if defining environmental densities with a mass complete sample. We postpone a more detailed investigation of this issue to a forthcoming paper. As of today, only a photometric redshift survey like COSMOS, because of the high statistic available, may in fact allow such an investigation.

Cassata et al. (2007) analyzed a sample of 2041 galaxies with photometric redshifts within  $0.61 < z < 0.85$  and covering an area of 270 arcmin<sup>2</sup>, which is about nine times smaller than the one we use here. The accuracy of their photometric redshifts is comparable to the one in this work (see Mobasher et al. 2007). They perform a morphological classification up to  $I_{AB} < 24$ , thus the same flux limit we use in our analysis, using a set of nonparametric measurements of the galaxy light distribution (Conselice 2003; Abraham et al. 2003; Lotz et al. 2004). Also, following Dressler (1980) they estimate galaxy projected densities. They do find a well defined morphology–density relation in place and also a clear separation between early and late types, in all environments, in the stellar mass versus  $V - z$  observed color plane, with bulge-dominated galaxies sitting mainly in the red sequence and disk-dominated ones populating the blue cloud. Furthermore, they fit and discuss extensively the different slopes of the blue-cloud (late-type galaxies) and the red-sequence (early-type galaxies) distributions. We see similar characteristics in our data but, in our opinion, this is an effect mostly due to the sample mass completeness. As it is clear by looking at the mid column of Figure 10, the pronounced slope of the late-type galaxies distribution, compared to the bulge-dominated galaxy population, is mostly drawn by the mass completeness: red objects with such low mass, if existing, would have an  $I$ -band magnitude fainter than 24.

Nonetheless, their main results are in excellent agreement with the one presented in this work at  $z \approx 0.7$ , in spite of the different ways used to estimate galaxy environmental properties.

#### 7.4. The Specific Star Formation Rate

One way to explore the contribution of star formation to the stellar mass growth in galaxies of different mass is to study the redshift evolution of the specific SFR (SSFR), which is defined as the SFR per unit stellar mass. A number of works in the last years (e.g., Brinchmann & Ellis 2000; Feulner et al. 2005a, 2005b; Bauer et al. 2005; Iglesias-Páramo et al. 2007; Zheng et al. 2007; Cowie & Barger 2008; Damen et al. 2009; Dunne et al. 2009; Santini et al. 2009; Pannella et al. 2009) have focused on the SSFR redshift evolution, consistently finding an increase of the mean SSFRs with redshift.

Following Madau et al. (1998), the SFR of individual objects can be estimated from the rest-frame UV luminosity as  $SFR_{2800} = 1.27 \times 10^{-28} \times L_{2800}$  in units of  $M_{\odot} \text{ yr}^{-1}$ , where the constant factor is computed for a Salpeter IMF. The SFR of each galaxy is corrected by the dust attenuation obtained for the SED fitting using the extinction curve of Calzetti et al. (1994).

In Figure 11 we present the SSFR as a function of stellar mass and morphology, in three redshift ranges up to redshift 1.15, and in different environments. The figure shows contour isodensity levels drawn as in Figure 10.

Before discussing in some detail Figure 11, we would like to first discuss some evident similarities with Figure 10. The rest-frame  $U - B$  color is bracketing the Balmer break of a galaxy spectrum, hence is mostly sensitive to the age of the galaxy stellar population (e.g., Gallazzi et al. 2005). To convert an age in a SFR, one needs, to first order and neglecting the dust attenuation correction, to normalize it to the underlying continuum emission or to the galaxy stellar mass i.e.:  $\log SFR \propto -(U - B) + \log M_{*}$ . Taking this into account one can, again roughly speaking, link the two plots with the following conversion:  $\log SSFR \propto -(U - B)$ . With this simple conversion in mind, it is easier to understand why there are so many similarities between the two figures.

In both figures the red and blue clouds are very well separated, at all redshifts and in all environments. This is more pronounced in high-density environments, while going to lower density regions there is clear trend of the low-mass early types to head toward high SSFRs, or bluer  $U - B$  color, values. These galaxies are young blue bulge-dominated galaxies with high star formation activity and stellar masses of order a few times  $10^9$  solar masses.

The intermediate-type galaxies fall in between, again confirming their nature of transition objects. It is worth noting though that while they overlap with the low-mass star-forming late-type population at all redshifts and in all environments, they tend to leave the high-mass end at progressively lower redshifts.

Coming more specifically to Figure 11, the location in the SSFR versus stellar mass plot of the maximum galaxy density of the early-type population, is increasing its star formation by not more than a factor of 3 over the explored redshift range, while the blue cloud is moving by approximately a factor of 10 in the same redshift range. The two clouds are pretty much segregated in mass: while late-types are always dominating at low masses, the early- and intermediate-type objects completely dominate the high-mass tail. This mass segregation gets definitely stronger in denser environments.

The upper envelope of the SSFR is running essentially parallel to lines of constant SFR, and it is shifting to higher SFRs with

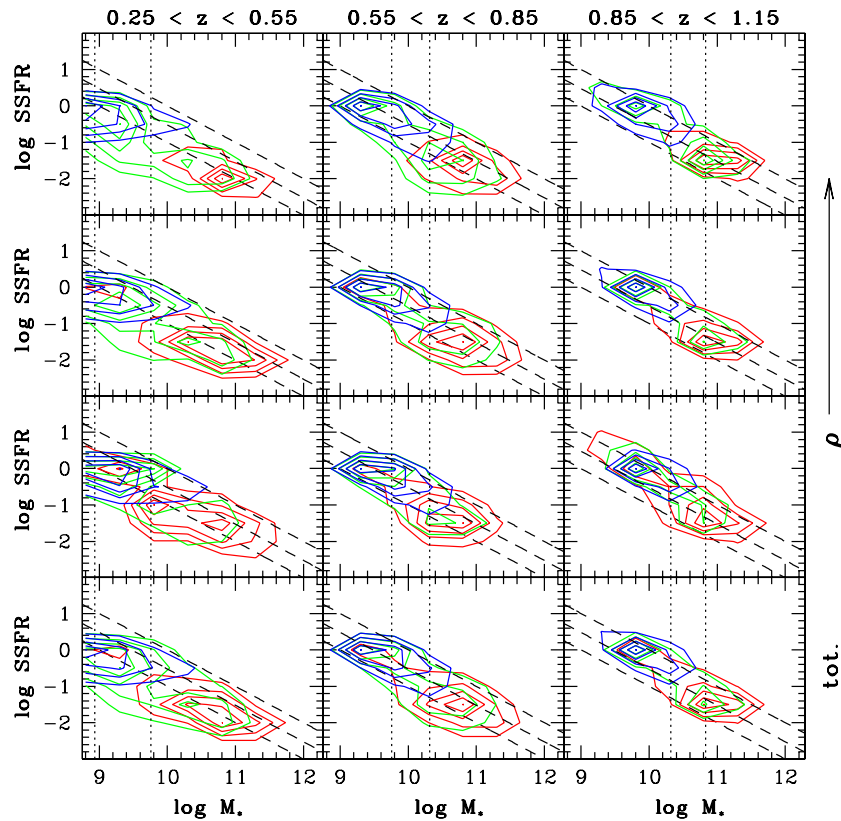


**Figure 11.** SSFR as a function of stellar mass and morphology for three different redshift bins and in different environments. Contours define the morphological classes and are drawn as explained in the text. The tilted dotted dashed represent constant SFRs of 1, 3, and  $10 M_{\odot} \text{ yr}^{-1}$  and they are supposed to guide the eye. The bottom row shows the total value. The two vertical dotted lines show the mass completeness values at the upper and lower edges of each redshift bin.

increasing redshift, as it was already noted in earlier work. Note that this upper envelope is partly affected by a selection effect: heavily dust obscured starbursts cannot be detected in our sample.

Furthermore, it is evident that the most massive galaxies have the lowest amount of star formation per unit stellar mass up to the highest redshift probed, and hence they cannot have formed the bulk of their stars in this redshift range. This pushes the bulk of their star formation at earlier cosmic epochs, in agreement with the downsizing scenario (Cowie et al. 1996).

Caputi et al. (2008) analyzed a sample of 609 sources in the COSMOS field, with both optical spectra from the zCOSMOS-DR2 and a MIPS  $24\mu$  photometric measurement available. In their study they compared different kinds of SFR indicators, i.e., UV light, line emissions, and IR luminosity, thus allowing an investigation of the dust extinction affecting these diagnostics. As a main result, at least for what concerns our work here, they find that the Calzetti et al. (1994) attenuation law works well for dereddening both the UV light and the  $H_{\delta}$ ,  $H_{\alpha}$  line fluxes. Although the median  $A_V$  of our sample, as derived from the SED fitting, turns out to be somewhat lower than the one they find for the MIPS  $24\mu$  selected sample, we note that this might be partially due to a selection effect of the Caputi et al. (2008) sample. We postpone a more careful analysis of this issue to a future work, which will make use of the recently available *Spitzer Space Telescope* mid-infrared observations (Sanders et al. 2007).

In Figure 11, it is also worth noting the evolution of the SSFR as a function of the environment. At a first glance, there is not much difference between the different environments. Nonetheless, at all redshifts there is a tendency of

the early-type sample to present a plume toward the high SSFR zone, which is very pronounced at lower environmental densities.

## 8. DISCUSSION AND CONCLUSIONS

In this work we have studied the evolution of the stellar mass content of disk-dominated and bulge-dominated galaxies with respect to the total mass budget up to  $z \sim 1.2$ , and its dependence from the local environment.

As expected, we find that early-type objects always dominate the high-mass end, while at progressively lower stellar masses late-type objects increase their contribution to the total mass density.

At each redshift, a *transition mass* can be identified as the stellar mass where the transition from a bulge-dominated to a disk-dominated stellar mass budget takes place. Based on the good statistics available in this work, we are able to confirm that the morphological mix at the high-mass end evolves with cosmic time, with the transition mass increasing with redshift. At  $z \sim 0.7$  we find a transition mass approximately consistent with the local value  $M \approx 5 \times 10^{10} M_{\odot}$ , while at  $z \sim 1$  the late-types and early-types contributions become comparable at  $M \approx 1 \times 10^{11} M_{\odot}$ .

The stellar mass function of disk-dominated galaxies is consistent with being constant over the redshift range (0.3–1.2), with number densities declining by more than an order of magnitude in the mass range  $\log M_* = (10.6–12)$ . On the other hand, the stellar mass function of bulge-dominated systems shows a pure normalization decline with redshift. Such different behavior of the stellar mass functions of late-type and early-type

galaxies naturally sets the redshift evolution of the transition mass.

The slope of total number density evolution with redshift is consistent, within the errors, with being the same in all mass ranges, at least up to the common redshift completeness. This means that the galaxy stellar mass function, in the redshift range and stellar mass range explored, does not evolve in shape but only in normalization with redshift (see also Marchesini et al. 2008 for similar conclusions at higher redshifts). According to our data we do not see any differential evolution between the high-mass and the low-mass end of the galaxy stellar mass function.

We have identified in the photometric redshift distribution a large-scale structure underdensity at  $z \approx 0.5$ . It gets more and more significant with increasing stellar mass. The morphological evolution in this underdense redshift bin is *delayed* at all stellar masses: the early-type fraction, both with respect to the total number density and to the late-type number density, is much lower than those in the contiguous redshift bins, in agreement with the expectations of the morphology–density relation. We note that the morphological mix in this underdense redshift bin is, at all masses probed, very close to the morphological mix at  $z \approx 1.1$ , which has a comparable total comoving number density of objects.

We further explored the redshift evolution of the galaxy stellar mass function split by morphology and by environmental density. In overdense and medium-dense environments, the mass function shape is in good agreement with local determinations. However, we find that the slope of the mass function is anti-correlated with the environmental density: the less dense is the environment the more steep is the mass function. This trend has also been found locally by Baldry et al. (2006).

In overdense regions, at all redshifts probed, a very massive early-type population seems to exist, which overcomes the local *field* mass function determination: we might be witnessing the appearance of giant elliptical galaxies in the highest density regions.

The morphologically split mass content evolves with both redshift and local density, with a striking feature: at different redshifts, the morphological mix and the transition mass appear to mainly depend on the local number density.

We have presented both the fraction of early-type galaxies with respect to the total galaxy population and the ratio between early- to late-type objects at different redshifts and for different environments, finding that a morphology–density relation is already well in place at redshift 1.

We have found that early- and late-type galaxies in the stellar mass versus SSFR plane (or stellar mass vs. rest-frame  $U - B$  color) are well separated at all redshifts and in all environments. The intermediate-type galaxies fall in between, confirming their nature of transition objects. At increasing redshift, the peak of the early-type galaxy distribution in such a plane is moving toward higher SSFR by a factor of  $\leq 3$ . At the same time, the peak of the late-type galaxy distribution shifts by approximately a factor of 10 in the same redshift range.

The early- and late-type galaxy populations exhibit a significant segregation in mass: late-type galaxies dominate at low masses while early-type and intermediate objects dominate the high-mass tail. Therefore, early-type and intermediate galaxies drive the evolution of star formation present in massive ( $\geq 7 \times 10^{10} M_{\odot}$ ) galaxies, while lower mass disk-dominated galaxies are mostly responsible for the global decline of the cosmic star formation from redshift 1 to the local universe.

While in general this picture seems to be quite similar in all environments, in low-density regions there is a population of relatively massive, early-type galaxies, having high SSFR and blue colors.

We also explored, with the highly homogeneous data set available, the age of the massive early-type galaxy stellar populations as a function of environment. The massive early-type galaxies have similar characteristic ages, colors, and SSFRs, hence a similar formation redshift independently of the environment they belong to. The age distributions in different environments show a difference in the mean ages (neglecting the age–metallicity degeneracy) which is in a good agreement with published results.

Finally, in agreement with previous work, we have found that the galaxies hosting the oldest stars in the universe preferentially belong to the highest density regions.

We thank the anonymous referee for constructive comments which helped us to improve significantly the presentation of our results. M.P. and V.S. are grateful for support from the Max-Planck Society and the Alexander von Humboldt Foundation. Part of this work was supported by the German *Deutsche Forschungsgemeinschaft*, DFG SFB 375. M.P. thanks Gabriella De Lucia, Daniele Pierini, and Stefano Zibetti for a careful reading of the manuscript and for many insightful comments and suggestions. We gratefully thank the entire COSMOS Collaboration for the huge amount of work and high-quality data released to the whole community. The *HST* COSMOS Treasury program was supported through NASA grant HST-GO-09822. More information on the COSMOS survey is available at <http://www.astro.caltech.edu/cosmos>. The National Radio Astronomy Observatory is a facility of the National Science Foundation operated under cooperative agreement by Associated Universities, Inc. This work is based in part: (1) on observations obtained with MegaPrime/MegaCam, a joint project of CFHT and CEA/DAPNIA, at the Canada–France–Hawaii Telescope (CFHT) which is operated by the National Research Council (NRC) of Canada, the Institut National des Science de l'Univers of the Centre National de la Recherche Scientifique (CNRS) of France, and the University of Hawaii; and (2) on data products produced at TERAPIX and the Canadian Astronomy Data Centre as part of the Canada–France–Hawaii Telescope Legacy Survey, a collaborative project of NRC and CNRS. This research has made use of the NASA/IPAC Infrared Science Archive, which is operated by the Jet Propulsion Laboratory, California Institute of Technology, under contract with the National Aeronautics and Space Administration.

## APPENDIX A

### THE MORPHOLOGICAL ANALYSIS

In the following, we describe the analysis aimed at quantitatively determine the morphological properties of the galaxy sample we use in this work. The morphological analysis is based on the ACS imaging of the COSMOS field in the F814W passband, and was performed on all galaxies in our sample down to a limit of  $F814W = 24$ .

We explain below the details of the adopted procedure and the tests that were performed to assess the robustness of our results.

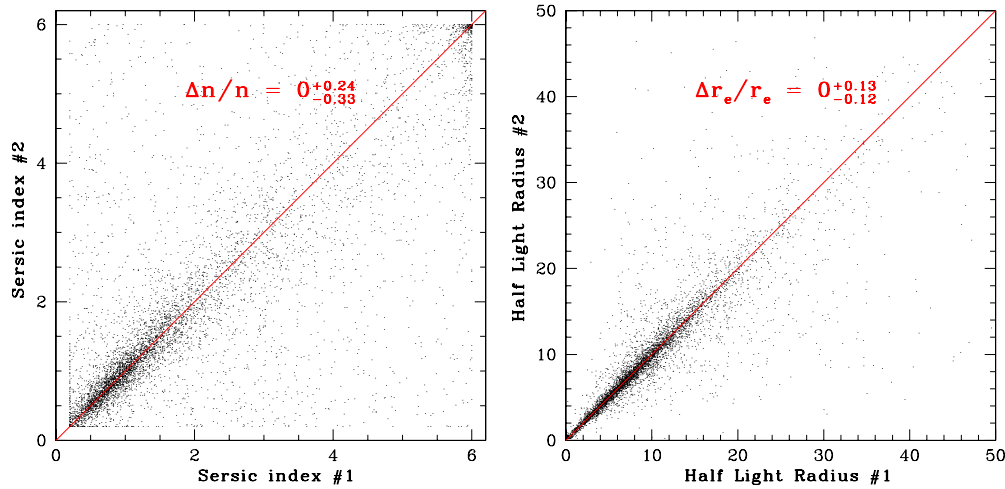


**Figure 12.** Comparison of morphological parameters obtained by fitting the surface brightness of all sources falling in two distinct ACS tiles. For each object, the fit was performed on both images, and the resulting Sérsic indices and effective radii are compared in the left and right panels, respectively. The recovered median and 16th, 84th percentiles of the  $\Delta n/n$  and  $\Delta r/r$  distributions are inserted in the two panels.

(A color version of this figure is available in the online journal.)

### A.1. Fitting Sérsic Profiles with GIM2D

We use the package GIM2D (Simard et al. 1999) to fit PSF convolved Sérsic (1968) profiles to the two-dimensional surface brightness distribution of each galaxy:

$$\Sigma(r) = \Sigma_e e^{-\kappa[(r/r_e)^{1/n} - 1]}, \quad (\text{A1})$$

where  $r_e$  is the effective radius of the galaxy,  $\Sigma_e$  is the surface brightness at  $r_e$ ,  $n$  is the power-law index (Sérsic index), and  $\kappa$  is coupled to  $n$  such that half of the total flux is always within  $r_e$ . For  $n \gtrsim 2$ ,  $\kappa \approx 2n - 0.331$ ; at low  $n$ ,  $\kappa(n)$  flattens out toward 0 and is obtained by interpolation. The adjustable form of the Sérsic law has the advantage of parameterizing, through the variable exponent  $n$ , surface brightness distributions including the exponential radial falloff of the light profile in bulgeless disks ( $n = 1$ ), and the classical de Vaucouleur profile typical of elliptical galaxies ( $n = 4$ ).

During the fitting process, the model is convolved with the user specified PSF, and then compared to the input image. When fitting a single Sérsic model, GIM2D seeks the best-fitting values for the following eight parameters: total flux, half-light radius, ellipticity, position angle, center of the galaxy, background level, and value of the Sérsic index.

### A.2. PSF Influence on the Morphological Parameters

The accurate determination of the image PSF is important for the proper determination of the morphological parameters. The PSFs used to convolve the profiles were obtained for each individual ACS tile by stacking about 10 high S/N isolated stars.

Although we did not expect the outcome of single Sérsic fits to depend strongly on small variations of the PSF, we carried out some tests with varying PSFs on a few COSMOS tiles to assess the influence of the PSF on the retrieved morphological parameters. Such tests were performed by using: (1) a single universal PSF obtained by stacking all the COSMOS high S/N isolated stars; (2) the PSF we derived for the FDF in Pannella et al. (2006), which was observed in the same filter F814W and at almost the same depth as COSMOS. We found that the largest differences obtained in the output parameters were of

order 3%–5%, meaning that single Sérsicfits are pretty robust against such PSF variations.

We also tested the accuracy of the PSF itself by fitting all the point-like sources as selected with the SExtractor catalog parameters. Specifically, we used the neural network star classifier (CLASS\_STAR), the half-light radius, and the FWHM, to identify point-like sources. When GIM2D-fitting such point-like sources, the vast majority—but the saturated stars—has a best-fit half-light radius smaller than 0.01 pixel, meaning that after the code convolves them with the provided PSF they are indeed recovered as point-like sources.

### A.3. Results on the Overlapping COSMOS ACS Tiles

Since the COSMOS ACS tiles are slightly overlapping, we took advantage of this feature to further test the reliability of our fitting procedure as well as to assess many other possible systematics, like for instance PSF variation in time and over the ACS field of view, or photometric and astrometric distortion.

All sources appearing in two tiles were fitted separately in each tile, and the fit results were compared. The outcome of this test is shown in Figure 12, where we plot one against the other the GIM2D output (Sérsic index and half-light radius) coming from the two fits for all such objects ( $\approx 8000$ ). An overall accuracy of  $\Delta n/n \sim 0.3$  and  $\Delta r/r \sim 0.1$  is obtained. Taking into account that in the tile borders only three out of four dithers are overlapping, and hence that the image rms is greater than in the central part of the image, one should consider these uncertainties as safe upper limits.

### A.4. Results on Simulated Objects

We further tested the accuracy of our analysis by running GIM2D on simulated images. This test was performed by adding 3000 fake objects, one at a time, to the real image, in a blank, pure-sky region. The simulated galaxies were generated with the GIM2D task *gsimul*, by adding on the selected pure-sky region objects with structural parameters uniformly distributed in specified ranges (magnitude in (22.5–24), ellipticity in (0.1–0.9), position angle in (0–90), effective radius in (0–60 pixel), Sérsic index in (0.2–6)). Each single object is first added into the image, then it is extracted with the same

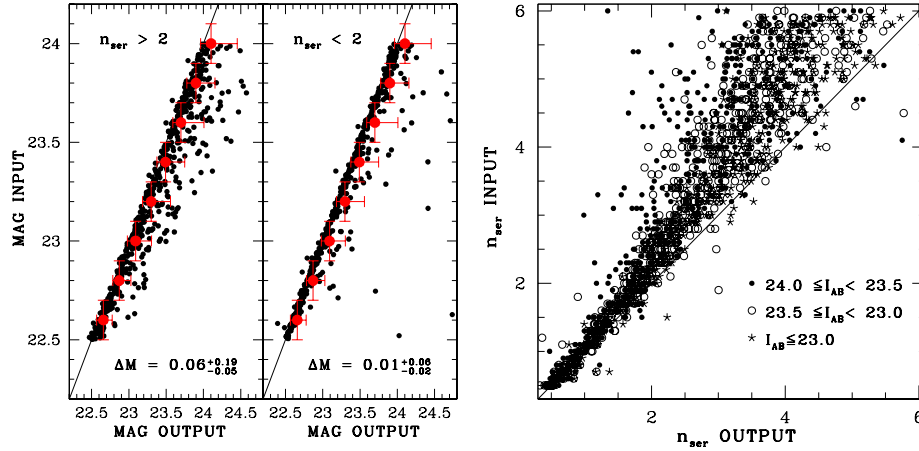


**Figure 13.** Left: output GIM2D recovered vs. input simulated magnitudes are shown for objects with  $n_{\text{ser}} > 2$  (left) and  $n_{\text{ser}} < 2$  (right). In each panel the median differences with errors are shown. Right: GIM2D recovered  $n_{\text{ser}}$  vs. simulated ones. High Sérsic index objects with magnitudes in the range 23/24, despite being easily detectable, fall with their extended wings under the sky surface brightness and suffer from a recovered lower value. (A color version of this figure is available in the online journal.)

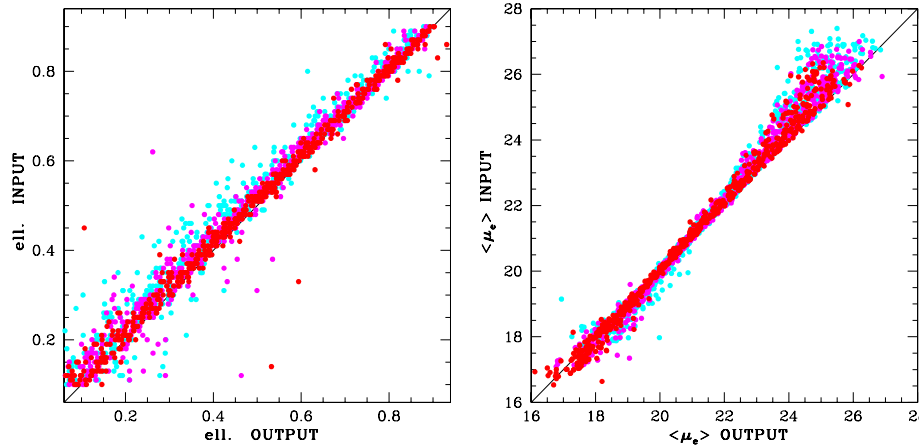


**Figure 14.** GIM2D test results on simulated objects. The plots show the output vs. input ellipticity (left panel) and  $\mu_e$  (right panel). Points are colored according to the simulated objects total magnitudes in red ( $I < 22.5$ ), magenta ( $22.5 < I < 23.5$ ), and cyan ( $23.5 < I < 24$ ). (A color version of this figure is available in the online journal.)

SExtractor configuration file used for the real images. It is then analyzed from GIM2D exactly as done for the real objects. The input magnitudes are generally better recovered for objects with  $n_{\text{ser}} \lesssim 2$  than for objects with  $n_{\text{ser}} \gtrsim 2$ , with a median  $\Delta M = 0.01$  and  $0.06$ , respectively (see the left panel of Figure 13). High Sérsic index objects have very extended wings that, depending on the total flux, can fall under the sky surface brightness, thus for these objects a lower Sérsic index, the total flux and effective radii are usually recovered (see the right panel of Figure 13). We find that the profile parameters of simulated objects are well-recovered down to  $F814W = 24$  (see Figure 14). The recovered ellipticity and position angle, as compared to the input ones, show no trends with magnitude and are generally very well recovered (see the left panel of Figure 14 for the ellipticity).

#### A.5. GIM2D versus GALFIT

We tested our results by running also the GALFIT (Peng et al. 2002) code on four of the COSMOS ACS patches. GALFIT is a two-dimensional galaxy fitting software package more recent than GIM2D, and it was designed to extract many structural components from galaxy images. It is very flexible and able

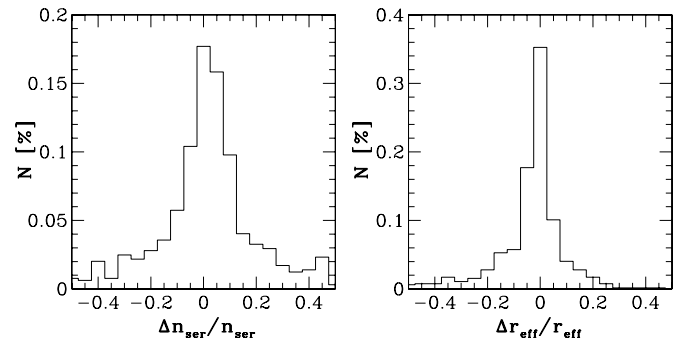


**Figure 15.** GIM2D vs. GALFIT comparison. In figure the distribution obtained, on four COSMOS tile, of  $\Delta n/n$  (left panel) and  $\Delta r/r$  (right panel) from the two codes. The median is 0 and the width is less than 0.2 for  $\Delta n/n$  and about 0.1 for  $\Delta r/r$ .

to fit an arbitrary number of galaxies simultaneously on an image, making it an ideal tool to fit neighboring objects in a sensitive way and not being biased from external informations such as the SExtractor segmentations used by GIM2D. During the fitting process, as for GIM2D, the model is convolved with the specified PSF, and then compared to the input image.

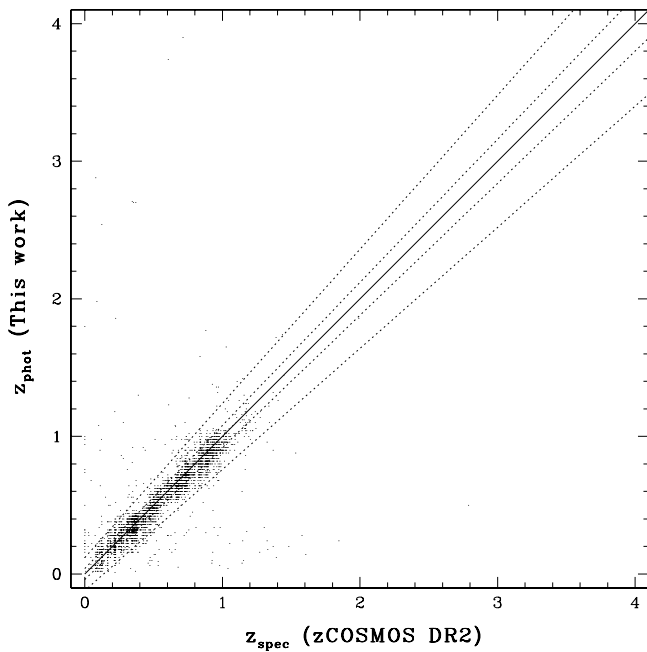


**Figure 16.** Comparison between the zCOSMOS DR2 spectroscopic redshifts catalog and the photometric redshifts catalog used in this work. The dotted lines represent 0.04 and 0.12 rms values, while the solid line is the bisector, see the text for details.

Figure 15 shows a comparison between the two codes. No systematics are present, the median differences for both the recovered Sérsic index and half-light radius are very close to zero. The scatter is about 20% for the Sérsic index and 10% for the half-light radius.

One can argue that the COSMOS field is not very crowded and that in more crowded fields one could see some systematic differences between the two codes. Still, a similar comparison on deep ACS images of the galaxy cluster A1689 (Halkola et al. 2006) for a sample of bright ( $I < 22.5$ ) red-sequence early-type galaxies, beside a few obvious cases for which GALFIT performed best, showed no significant systematics between the two codes (see also Häussler et al. 2007 for slightly different but still similar conclusions on the comparison between the

two codes). Of course these considerations apply only to single Sérsic fitting, no simulations and tests were done concerning bulge/disk decomposition.

## APPENDIX B

### PHOTOMETRIC REDSHIFTS ACCURACY

#### B.1. Comparison with zCOSMOS DR2

In Figure 16, we show the comparison between the photometric redshifts used in this work and the recently released zCOSMOS DR2 spectroscopic redshifts catalog (Lilly et al. 2007). 4506 objects are in common with our catalog. The distribution of  $\Delta z / (1 + z_{\text{spec}})$  has a median value of 0.01 and an rms of 0.04 with only 2.5% of the distribution having a *catastrophic* photometric redshift, i.e., a  $\Delta z / (1 + z_{\text{spec}})$  greater than 0.2. This nicely confirms the results described in Gabasch et al. (2008), which were obtained by using a much smaller spectroscopic redshifts sample.

#### B.2. Comparison with Ilbert et al. (2009)

In the left panel of Figure 17, we compare the photometric redshifts used in this work with the ones from the recently released Ilbert et al. (2009a) COSMOS Legacy catalog for a sample of 40,717 objects common to both catalogs. We note that not all the objects of our morphological catalog are matched because the Ilbert et al. (2009a) sample does not contain the photometric redshifts for all the X-ray sources detected in the XMM COSMOS images (Cappelluti et al. 2009). The relative accuracy between the two photometric redshift realizations is about 5%, which is in a good agreement with the one expected from the absolute errors quoted in the two studies. Finally, only 4% of the common objects have photometric redshifts that differ by more than 20%.

In the right panel of Figure 17, we show the redshift distribution of our sample obtained using the Ilbert et al. (2009a) catalog (dotted line) as compared to the one we are using in the work (solid line, see Figure 1). We note that the two distributions agree very well, including the detection of the large-scale structure underdensity at  $z \sim 0.5$ .

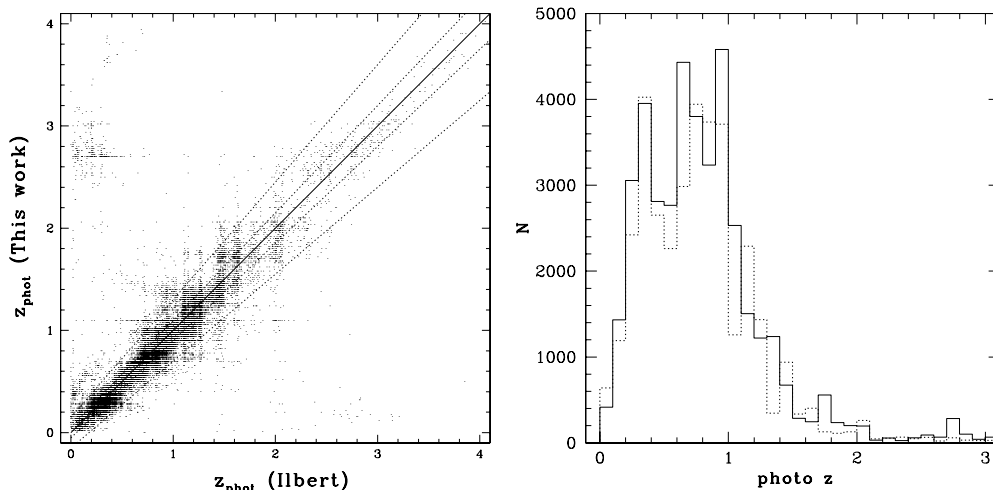


**Figure 17.** Left: comparison between the photometric redshift catalog used in this work and the one recently published from Ilbert et al. (2009a). The dotted lines represent 0.05 and 0.15 rms values, while the solid line is the bisector. Right: comparison between the photometric redshift distribution (solid line) used in this work (as in Figure 1) and the one (dotted line) from the Ilbert et al. (2009a) catalog for the very same sample.

## REFERENCES

- Abraham, R. G., van den Bergh, S., & Nair, P. 2003, *ApJ*, **588**, 218
- Abraham, R. G., et al. 1996, *MNRAS*, **279**, L47
- Abraham, R. G., et al. 2007, *ApJ*, **669**, 184
- Arnouts, S., et al. 2007, *A&A*, **476**, 137
- Baldry, I. K., et al. 2004, *ApJ*, **600**, 681
- Baldry, I. K., et al. 2006, *MNRAS*, **373**, 469
- Bamford, S. P., et al. 2009, *MNRAS*, **393**, 1324
- Barden, M., et al. 2005, *ApJ*, **635**, 959
- Bauer, A. E., Drory, N., Hill, G. J., & Feulner, G. 2005, *ApJ*, **621**, L89
- Bell, E. F., McIntosh, D. H., Katz, N., & Weinberg, M. D. 2003, *ApJS*, **149**, 289
- Bender, R., Burstein, D., & Faber, S. M. 1992, *ApJ*, **399**, 462
- Bender, R., et al. 2001, in *ESO/ECF/STScI Workshop on Deep Fields*, ed. S. Christiani (Berlin: Springer), 327
- Benítez, N., et al. 2004, *ApJS*, **150**, 1
- Bertin, E., & Arnouts, S. 1996, *A&AS*, **117**, 393
- Blakeslee, J. P., et al. 2006, *ApJ*, **644**, 30
- Blanton, M. R., et al. 2003, *ApJ*, **592**, 819
- Borch, A., et al. 2006, *A&A*, **453**, 869
- Bouwens, R. J., Illingworth, G. D., Franx, M., & Ford, H. 2007, *ApJ*, **670**, 928
- Bouwens, R. J., et al. 2004, *ApJ*, **606**, L25
- Bower, R. G., Benson, A. J., & Malbon, R., et al. 2006, *MNRAS*, **370**, 645
- Brimouille, F., Lerchster, M., Seitz, S., Bender, R., & Snigula, J. 2008, arXiv:0811.3211
- Brinchmann, J., & Ellis, R. S. 2000, *ApJ*, **536**, L77
- Bruzual, G., & Charlot, S. 2003, *MNRAS*, **344**, 1000
- Bundy, K., Ellis, R. S., & Conselice, C. J. 2005, *ApJ*, **625**, 621
- Bundy, K., et al. 2006, *ApJ*, **651**, 120
- Calzetti, D., Kinney, A. L., & Storchi-Bergmann, T. 1994, *ApJ*, **429**, 582
- Caon, N., Capaccioli, M., & D'Onofrio, M. 1993, *MNRAS*, **265**, 1013
- Capak, P., et al. 2007a, *ApJS*, **172**, 284
- Capak, P., et al. 2007b, *ApJS*, **172**, 99
- Cappelluti, N., et al. 2009, *A&A*, **497**, 635
- Caputi, K. I., et al. 2008, *ApJ*, **680**, 939
- Cassata, P., et al. 2007, *ApJS*, **172**, 270
- Cattaneo, A., Dekel, A., Faber, S. M., & Guiderdoni, B. 2008, *MNRAS*, **389**, 567
- Cimatti, A., Daddi, E., & Renzini, A. 2006, *A&A*, **453**, L29
- Cimatti, A., et al. 2008, *A&A*, **482**, 21
- Cole, S., Lacey, C. G., Baugh, C. M., & Frenk, C. S. 2000, *MNRAS*, **319**, 168
- Cole, S., et al. 2001, *MNRAS*, **326**, 255
- Conselice, C. J. 2003, *ApJS*, **147**, 1
- Cooper, M. C., Tremonti, C. A., Newman, J. A., & Zabludoff, A. I. 2008, *MNRAS*, **390**, 245
- Cowie, L. L., & Barger, A. J. 2008, *ApJ*, **686**, 72
- Cowie, L. L., Songaila, A., Hu, E. M., & Cohen, J. G. 1996, *AJ*, **112**, 839
- Cox, T. J., Younger, J., Hernquist, L., & Hopkins, P. F. 2008, in *IAU Symp. 245, Formation and Evolution of Galaxy Bulges*, ed. M. Bureau, E. Athanassoula, & B. Barbuy (Dordrecht: Kluwer), 63
- Croton, D. J., et al. 2005, *MNRAS*, **356**, 1155
- Cucciati, O., et al. 2006, *A&A*, **458**, 39
- Damen, M., et al. 2009, *ApJ*, **690**, 937
- Dekel, A., et al. 2009, *Nature*, **457**, 451
- De Lucia, G., Springel, V., White, S. D. M., Croton, D., & Kauffmann, G. 2006, *MNRAS*, **366**, 499
- de Vaucouleurs, G. 1948, *Ann. Astrophys.*, **11**, 247
- de Vaucouleurs, G., et al. 1991, *Third Reference Catalogue of Bright Galaxies* (Berlin: Springer) (Volume 1–3)
- Dickinson, M., Papovich, C., Ferguson, H. C., & Budavári, T. 2003, *ApJ*, **587**, 25
- Djorgovski, S., & Davis, M. 1987, *ApJ*, **313**, 59
- Dressler, A. 1980, *ApJ*, **236**, 351
- Dressler, A., et al. 1987, *ApJ*, **313**, 42
- Drory, N., & Alvarez, M. 2008, *ApJ*, **680**, 41
- Drory, N., Bender, R., & Hopp, U. 2004a, *ApJ*, **616**, L103
- Drory, N., et al. 2004b, *ApJ*, **608**, 742
- Dunne, L., et al. 2009, *MNRAS*, **394**, 3
- Feulner, G., Goranova, Y., Drory, N., Hopp, U., & Bender, R. 2005a, *MNRAS*, **358**, L1
- Feulner, G., et al. 2005b, *ApJ*, **633**, L9
- Fontana, A., et al. 2004, *A&A*, **424**, 23
- Fontana, A., et al. 2006, *A&A*, **459**, 745
- Fontanot, F., De Lucia, G., Monaco, P., Somerville, R. S., & Santini, P. 2009, arXiv:0901.1130
- Ford, H. C., et al. 2003, *Proc. SPIE*, **4854**, 81
- Franceschini, A., et al. 2006, *A&A*, **453**, 397
- Freeman, K. C. 1970, *ApJ*, **160**, 811
- Gabasch, A., Goranova, Y., Hopp, U., Noll, S., & Pannella, M. 2008, *MNRAS*, **383**, 1319
- Gabasch, A., et al. 2004a, *A&A*, **421**, 41
- Gabasch, A., et al. 2004b, *ApJ*, **616**, L83
- Gallazzi, A., Charlot, S., Brinchmann, J., White, S. D. M., & Tremonti, C. A. 2005, *MNRAS*, **362**, 41
- Gehrels, N. 1986, *ApJ*, **303**, 336
- Giallongo, E., et al. 2005, *ApJ*, **622**, 116
- Giavalisco, M., et al. 2004, *ApJ*, **600**, L93
- Gobat, R., et al. 2008, *A&A*, **488**, 853
- Graham, A. W., Trujillo, I., & Caon, N. 2001, *AJ*, **122**, 1707
- Halkola, A., Seitz, S., & Pannella, M. 2006, *MNRAS*, **372**, 1425
- Häussler, B., et al. 2007, *ApJS*, **172**, 615
- Heidt, J., et al. 2003, *A&A*, **398**, 49
- Hopkins, P. F., Cox, T. J., Kereš, D., & Hernquist, L. 2008, *ApJS*, **175**, 390
- Iglesias-Páramo, J., et al. 2007, *ApJ*, **670**, 279
- Ilbert, O., et al. 2009a, *ApJ*, **690**, 1236
- Ilbert, O., et al. 2009b, arXiv:0903.0102
- Kitzbichler, M. G., & White, S. D. M. 2007, *MNRAS*, **376**, 2
- Koekemoer, A. M., et al. 2007, *ApJS*, **172**, 196
- Leauthaud, A., et al. 2007, *ApJS*, **172**, 219
- Lee, J. 2006, *ApJ*, **644**, L5
- Le Fèvre, O., et al. 2005, *A&A*, **439**, 845
- Lilly, S. J., et al. 2007, *ApJS*, **172**, 70
- Lisker, T. 2008, *ApJS*, **179**, 319
- Lotz, J. M., Primack, J., & Madau, P. 2004, *AJ*, **128**, 163
- Madau, P., Pozzetti, L., & Dickinson, M. 1998, *ApJ*, **498**, 106
- Marchesini, D., et al. 2008, arXiv:0811.1773
- McIntosh, D. H., et al. 2005, *ApJ*, **632**, 191
- Mobasher, B., et al. 2007, *ApJS*, **172**, 117
- Mobasher, B., et al. 2009, *ApJ*, **690**, 1074
- Mouhcine, M., Baldry, I. K., & Bamford, S. P. 2007, *MNRAS*, **382**, 801
- Pannella, M., et al. 2006, *ApJ*, **639**, L1
- Pannella, M., et al. 2009, *ApJ*, **698**, 116
- Peng, C. Y., Ho, L. C., Impey, C. D., & Rix, H.-W. 2002, *AJ*, **124**, 266
- Pérez-González, P. G., et al. 2008, *ApJ*, **675**, 234
- Pozzetti, L., et al. 2007, *A&A*, **474**, 443
- Ravindranath, S., et al. 2004, *ApJ*, **604**, L9
- Rettura, A., et al. 2008, arXiv:0806.4604
- Rix, H.-W., et al. 2004, *ApJS*, **152**, 163
- Rudnick, G., et al. 2003, *ApJ*, **599**, 847
- Salpeter, E. E. 1955, *ApJ*, **121**, 161
- Sanders, D. B., et al. 2007, *ApJS*, **172**, 86
- Santini, P., et al. 2009, arXiv:0905.0683
- Sargent, M. T., et al. 2007, *ApJS*, **172**, 434
- Sawicki, M., & Thompson, D. 2006, *ApJ*, **648**, 299
- Scarlata, C., et al. 2007a, *ApJS*, **172**, 406
- Scarlata, C., et al. 2007b, *ApJS*, **172**, 494
- Scoville, N., et al. 2007a, *ApJS*, **172**, 38
- Scoville, N., et al. 2007b, *ApJS*, **172**, 1
- Sérsic, J. L. 1968, *Atlas de galaxias australes* (Cordoba: Observatorio Astronómico)
- Shen, S., et al. 2003, *MNRAS*, **343**, 978
- Simard, L., et al. 1999, *ApJ*, **519**, 563
- Smith, G. P., Treu, T., Ellis, R. S., Moran, S. M., & Dressler, A. 2005, *ApJ*, **620**, 78
- Somerville, R. S., et al. 2004, *ApJ*, **600**, L171
- Thomas, D., Maraston, C., Bender, R., & Mendes de Oliveira, C. 2005, *ApJ*, **621**, 673
- Trujillo, I., et al. 2004, *ApJ*, **604**, 521
- Trujillo, I., et al. 2006a, *MNRAS*, **373**, L36
- Trujillo, I., et al. 2006b, *ApJ*, **650**, 18
- Tully, R. B., & Fisher, J. R. 1977, *A&A*, **54**, 661
- van der Wel, A. 2008, *ApJ*, **675**, L13
- van Dokkum, P. G., & van der Marel, R. P. 2007, *ApJ*, **655**, 30
- van Dokkum, P. G., et al. 2008, *ApJ*, **677**, L5
- Williams, R. E., et al. 1996, *AJ*, **112**, 1335
- Willmer, C. N. A., et al. 2006, *ApJ*, **647**, 853
- Zamojski, M. A., et al. 2007, *ApJS*, **172**, 468
- Zheng, X. Z., et al. 2007, *ApJ*, **661**, L41